



Wireless closed-loop optogenetics across the entire dorsoventral spinal cord in mice

Claudia Kathe^{1,2,11}, Frédéric Michoud^{1,3,11}, Philipp Schönle^{4,11}, Andreas Rowald^{1,2}, Noé Brun⁴, Jimmy Ravier^{1,2}, Ivan Furfaro³, Valentina Paggi^{1,3}, Kyungjin Kim³, Sadaf Soloukey^{1,5,6}, Leonie Asboth^{1,2}, Thomas H. Hutson^{1,2}, Ileana Jelescu^{1,7}, Antoine Philippides⁸, Noaf Alwahab³, Jérôme Gandar^{1,2}, Daniel Huber⁸, Chris I. De Zeeuw^{5,9}, Quentin Barraud^{1,2}, Qiuting Huang⁴, Stéphanie P. Lacour^{1,3,12} ✉ and Grégoire Courtine^{1,2,10,12} ✉

Optoelectronic systems can exert precise control over targeted neurons and pathways throughout the brain in untethered animals, but similar technologies for the spinal cord are not well established. In the present study, we describe a system for ultrafast, wireless, closed-loop manipulation of targeted neurons and pathways across the entire dorsoventral spinal cord in untethered mice. We developed a soft stretchable carrier, integrating microscale light-emitting diodes (micro-LEDs), that conforms to the dura mater of the spinal cord. A coating of silicone-phosphor matrix over the micro-LEDs provides mechanical protection and light conversion for compatibility with a large library of opsins. A lightweight, head-mounted, wireless platform powers the micro-LEDs and performs low-latency, on-chip processing of sensed physiological signals to control photostimulation in a closed loop. We use the device to reveal the role of various neuronal subtypes, sensory pathways and supraspinal projections in the control of locomotion in healthy and spinal-cord injured mice.

Optogenetics has opened up unprecedented possibilities for controlling targeted cells and pathways of the nervous system with high spatiotemporal precision^{1–3}. The ability to dissect and manipulate the mechanisms underlying brain functions in health and disease has triggered the development of myriad systems to deliver photostimulation to peripheral nerves and the nerves in the brain^{4–12}.

The spinal cord is essential for the control of movement and many basic physiological functions. Unraveling the role of neurons and pathways embedded in the spinal cord is therefore a major endeavor in basic and clinical neuroscience. Compared with the brain, the spinal cord combines a series of unique challenges that require new light-delivery technologies^{6,9–11,13–17}. During natural behaviors, the spinal cord undergoes extensive displacements that are incompatible with penetrating optic fibers¹⁸. Consequently, the light must be delivered from sources positioned over the surface of the dura mater¹⁹. As the light rapidly scatters when penetrating spinal tissues, targeting deep intraspinal neurons with epidural light-emitting sources requires irradiances that are substantially higher than those required for photostimulation in the vicinity of targeted neurons or pathways. Such high-intensity illumination poses both technological and physiological challenges. Technologically, substantial irradiances require stable current flows delivered to the optoelectronic device despite miniaturized metallic

structures and movement-related mechanical stress. Physiologically, high irradiance leads to local heating of tissue due to light absorption, which may alter neuronal responses²⁰. Moreover, avoidance of tissue damage while ensuring efficient photostimulation requires embedding light-emitting sources within protective substrates that must conform to the topology, compliance and dynamics of spinal tissues. The poor accessibility and limited anchoring options of the vertebral column and spinal cord add a layer of complexity to the resolution of all these features^{6,13,14}. Indeed, spinal cord implants are prone to mechanical failure and poor biointegration⁹.

In the present study, we engineered a wireless optoelectronic system that possesses all the desired features for safe and long-term photostimulation of any targeted neurons and pathways in untethered and unrestricted mice. Moreover, we endowed the electronics with data acquisition and on-chip data-processing capabilities that enabled ultrafast closed-loop control of photostimulation using real-time processing of physiological signals.

Results

Topological and mechanical requirements for spinal implants.

We first collected the topological and mechanical requirements to ensure the long-lasting and safe integration of an optoelectronic implant over the entire extent of the mouse lumbar spinal cord. We acquired high-resolution magnetic resonance imaging

¹Center for Neuroprosthetics and Brain Mind Institute, School of Life Sciences, Swiss Federal Institute of Technology (EPFL), Geneva, Switzerland. ²Defitech Center for Interventional Neurotherapies (NeuroRestore), University Hospital Lausanne (CHUV), University of Lausanne and EPFL, Lausanne, Switzerland.

³Bertarelli Foundation Chair in Neuroprosthetic Technology, Laboratory for Soft Bioelectronic Interfaces, Institute of Microengineering, Institute of Biotechnology, Centre for Neuroprosthetics, EPFL, Geneva, Switzerland. ⁴Integrated Systems Laboratory, Department of Information Technology and Electrical Engineering, Swiss Institute of Technology Zurich, Zurich, Switzerland. ⁵Department of Neuroscience, Erasmus MC, Rotterdam, The Netherlands.

⁶Department of Neurosurgery, Erasmus MC, Rotterdam, The Netherlands. ⁷Centre d'Imagerie Biomedicale, EPFL, Lausanne, Switzerland. ⁸Department of Fundamental Neuroscience, University of Geneva, Geneva, Switzerland. ⁹Netherlands Institute of Neuroscience, Royal Dutch Academy of Arts and Sciences, Amsterdam, The Netherlands. ¹⁰Department of Neurosurgery, CHUV, Lausanne, Switzerland. ¹¹These authors contributed equally: Claudia Kathe, Frédéric Michoud, Philipp Schönle. ¹²These authors jointly supervised this work: Stéphanie P. Lacour, Grégoire Courtine. ✉e-mail: stephanie.lacour@epfl.ch; gregoire.courtine@epfl.ch

(MRI) and computed tomography (CT) datasets to generate a three-dimensional (3D) anatomical model of the mouse spinal cord and vertebral column (Extended Data Fig. 1 and Supplementary Video 1). We performed high-speed X-ray imaging (196 Hz) of freely behaving mice to capture the posture during standing, grooming and walking. We morphed the anatomical model on to these postures to quantify lumbar spine curvatures underlying ecological behaviors of mice (minimum bending radius of the spine = 5.13 cm; Extended Data Fig. 1 and Supplementary Video 1). These analyses outlined the suitable length (18 mm), width (2.5 mm) and thickness (<100 μm) of the implant to cover the rostrocaudal and mediolateral extents of the lumbar spinal cord, while providing quantified metrics on the required stretchability and conformability.

Design of the soft optoelectronic implant. We aimed to design an optoelectronic implant that is resilient to the demands of chronic implantation in the epidural space of mice, yet conformable to the curvilinear morphology of the soft spinal cord (Fig. 1a). To resolve this challenge, we combined thin-film microtechnology, elasticity engineering, micro-LEDs and dura-like silicone (Fig. 1b and Supplementary Video 1). We selected blue and green (wavelength, $\lambda = 470\text{ nm}$, $\lambda = 535\text{ nm}$) LEDs in a bare die format of small dimensions ($270 \times 220 \times 50\ \mu\text{m}^3$), which we interfaced with elastic serpentine titanium/gold/titanium (Ti/Au/Ti), interconnected and embedded in a poly(imide) film (Extended Data Fig. 2a). Each micro-LED was then coated with a silicone-phosphor composite⁸, before encapsulation of the entire array within a silicone membrane that matched the mechanical compliance of the natural dura mater¹⁸. This soft optoelectronic implant accommodates elongations (15% strain) that exceeded the physiological range of lumbar spinal cord displacements⁹. Reliable electrical properties for at least 30 d in accelerated aging conditions suggested that the optoelectronics would survive several weeks in vivo (Fig. 1d,e and Extended Data Fig. 2, step 5).

Electronics for recording and photostimulation. When conceiving the electronics to power the micro-LEDs and collect physiological signals, we intended to develop a wearable solution enabling the use of the same electronics in multiple mice and experiments.

We thus developed an ultraminiaturized, battery-powered, wearable, wireless recording and stimulation platform (1.1 g, 0.5 cm^3) that can be easily plugged on to a head-mounted connector interfaced with the micro-LED array. The platform was designed based on a customized integrated circuit system-on-chip for biomedical telemetry applications, termed VivoSoC3 (ref. ²¹) (Fig. 1f and Extended Data Fig. 3). The platform enables precise pulsed current control of two LED channels and recording from four pairs of electrodes. VivoSoC3 features a quad-core microcontroller unit (MCU) for low-latency, on-chip signal processing, which enables automated delivery of photostimulation based on acquired signals from physiological sensors. A 256-MB flash chip stores the acquired raw data and stimulation log values for offline analyses. The current delivered to each micro-LED can be configured independently over a

broad range of amplitudes (1–60 mA), frequencies (0.1–100 Hz), pulse widths (1–50 ms) and pulse repetitions (1–10,000) with fine resolution (1 mA, 0.1 Hz, 1 ms, 1 pulse repetition). Bluetooth communication enables fast, bidirectional and programmable control of each LED channel over distances exceeding 5 m in standard laboratory settings (Extended Data Fig. 3, step 3). The platform is operated via a handheld tablet that displays a real-time preview of the acquired physiological signals, the timing of the photostimulation and feedback on the accurate delivery of the configured current. The rechargeable battery of the detachable platform lasts for up to 11 h, including when data are streamed to the tablet in real time via Bluetooth, whereas photostimulation is controlled in the closed loop. In between experiments, the platform is plugged on to a USB-powered station for recharging.

Chronic biointegration of the soft optoelectronic implant. We next evaluated whether the mechanical properties of the micro-LED array met the static and dynamic requirements for long-term implantation in adult mice. The tailored dimensions of the implant (width: 2.5 mm; length: 1.8 cm; height: $100\ \mu\text{m}$) allowed smooth surgical insertion between the vertebrae and spinal cord (width: 4 mm; height: 0.12 mm) using a small laminotomy, that is, with minimal opening of the intervertebral/interlaminar space and without permanent attachment to the vertebrae (Extended Data Fig. 4 and Supplementary Video 1). CT reconstructions and MRI illustrated the conformability of the implant over the curved surface of the lumbar spinal cord (Fig. 2a,b). Quantification of foreign body responses based on the levels of glial fibrillary acidic protein and ionized calcium-binding adaptor molecule 1 (Iba1)¹⁸ confirmed the seamless biointegration of the micro-LED array within the spine for up to 6 weeks (Extended Data Fig. 4).

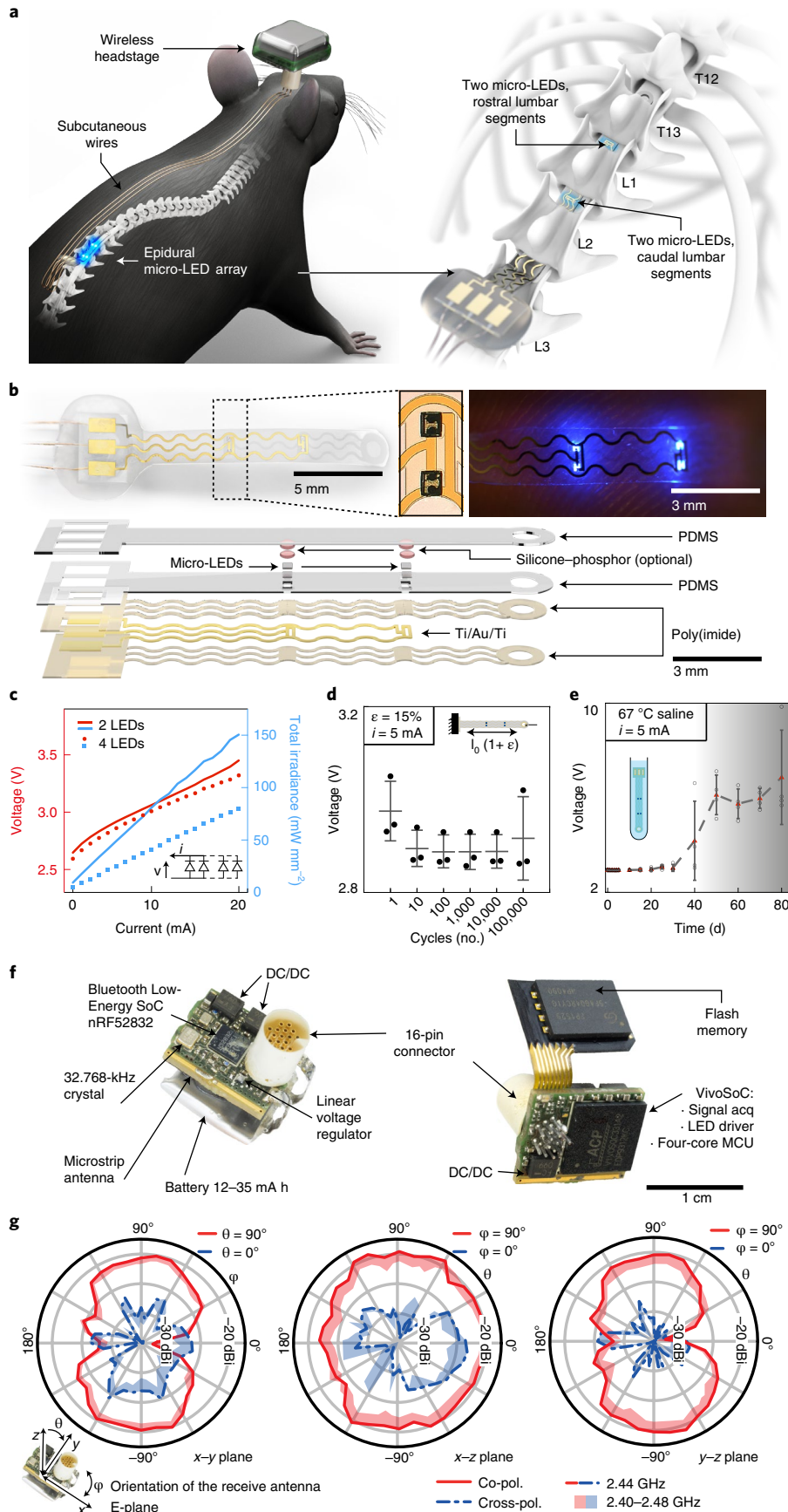
We then conducted a battery of tests to ask whether the spinal implant altered the natural behavior of the mice. We quantified locomotor performances using longitudinal recordings of whole-body kinematics during running and skilled locomotion. Quantification of these high-precision recordings using sensitive multifactorial statistical analyses²² revealed no measurable changes in gait patterns and balance performance ($n = 6$; Fig. 2c and Extended Data Fig. 5). Moreover, the micro-LED array had no impact on exploratory behaviors measured in an open field (Extended Data Fig. 5).

Long-term photostimulation in ecological environments. This optoelectronic system enabled real-time photostimulation of the spinal cord in ecological environments without the limitations of tethered electronics or spatial constraints of wireless radiofrequency powering. The mice executed classic behavioral paradigms, such as narrow beam walking, swimming in a large tank of water and climbing up a rope (Fig. 2d and Supplementary Video 1) while receiving remotely controlled photostimulation with millisecond precision (latency <15 ms). The optoelectronic system remained functional over the entire duration of the experiments (6 weeks). Failure analyses revealed that decline of photostimulation efficacy after longer experiments was not the result of issues with the micro-LED array,

Fig. 1 | Wireless optoelectronic system for closed-loop photostimulation of the lumbar spinal cord. **a**, Schematic overview of the optoelectronic system, including a zoom on the insertion of the micro-LED array over the epidural surface of the spinal cord. **b**, Photographs of the micro-LED array, including a zoom on the micro-LEDs and exploded diagram of the array. **c**, Optoelectronic characterization under incremental bias ($\lambda = 470\text{ nm}$). **d**, Stretchability. The optoelectronic implant was cycled at 15% strain, which corresponds to the range of motion of the lumbar spinal cord, for 100,000 cycles while continuously emitting light ($n = 3$, mean \pm s.e.m.). **e**, Accelerated aging. The optoelectronic implant was immersed in 67°C saline to accelerate degradation. The devices start failing around 40 d ($n = 4$, mean \pm s.e.m.). **f**, Photographs of the electronics embedded in the wireless, head-mounted platform that records physiological signals and powers the optoelectronics. **g**, In-air antenna radiation characteristics, measured in an anechoic chamber with a battery-operated, software-modified version of the headstage wireless device (emitting a carrier) and a linearly polarized (pol.) receive antenna. Drawn lines represent measurements at center frequency (2,440 MHz), whereas the shaded areas cover the full BLE bandwidth based on additional measurements at 2,400 MHz, 2,420 MHz and 2,480 MHz.

but of the oxidation of the subcutaneous copper wires connected to the headstage in the neck region. Indeed, X-ray imaging showed that this region undergoes extensive stress constraints during natural

behaviors (Extended Data Fig. 1). Over time, this continuous stress led to damage of the thin insulation layer (100- μm thick Teflon) and thus erosion of cooper wires (Extended Data Fig. 4).



Computational model of light penetration. The gray and white matter of the spinal cord present with dramatically different contents of light-diffracting, lipid-rich myelin. Consequently, spinal

tissues exhibit region-specific, light-penetration properties, suggesting that the position of the LEDs may play an important role in the efficiency of photostimulation, especially to reach deeply

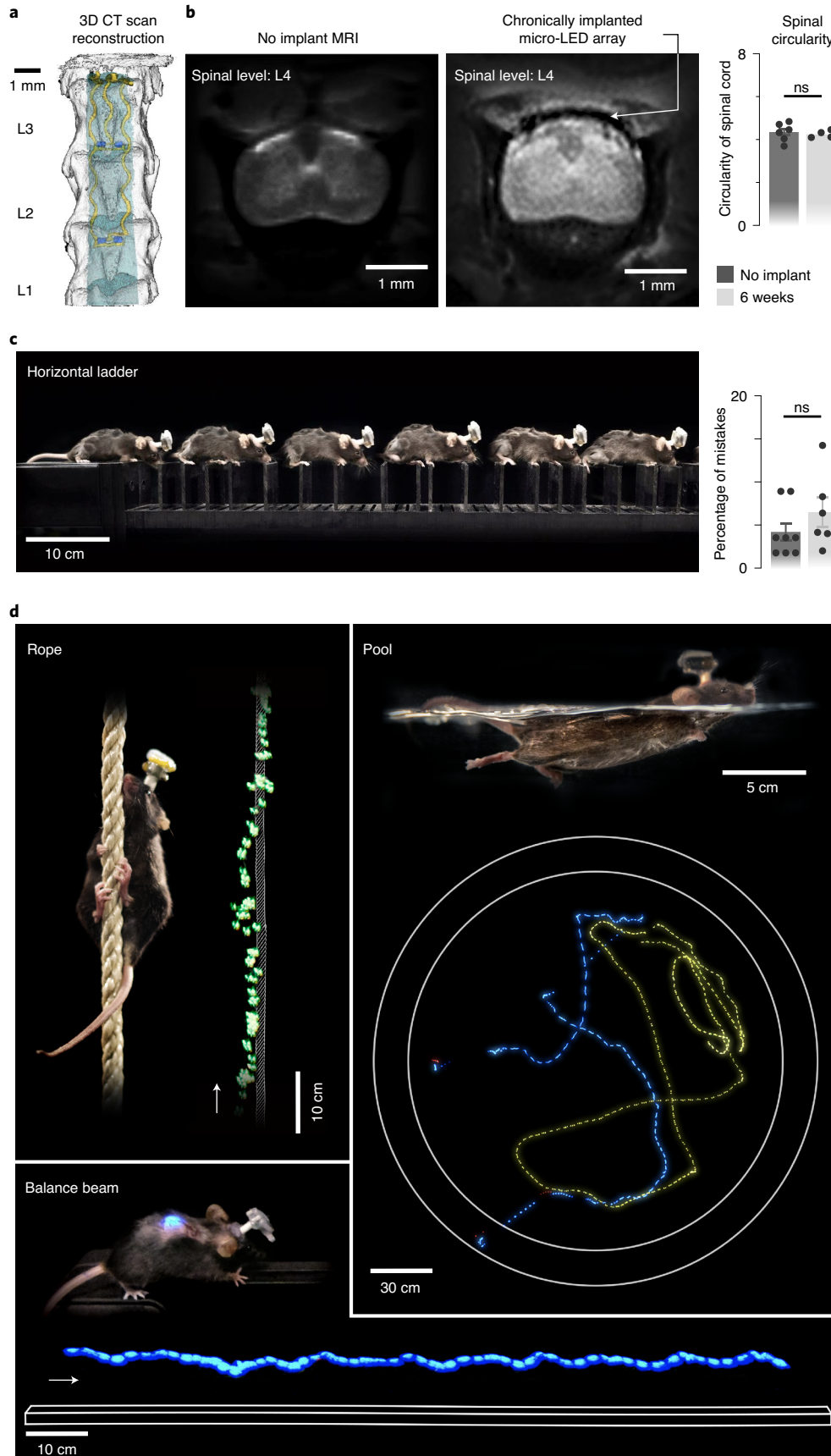


Fig. 2 | Long-term biointegration and photostimulation in ecological environments. **a**, The 3D rendering of the vertebrae T13–L3 and micro-LED array reconstructed from high-resolution CT scans. **b**, MRI of a spinal cord without and with an implanted micro-LED array. The bar graph reports the mean circularity of the spinal cord ($n=4-6$ mice, two-sided, unpaired Student's *t*-test, $P=0.67$, mean \pm s.e.m.). **c**, Chronophotography of a mouse walking freely and with precise paw placement along a horizontal ladder, despite the implanted micro-LED array and wearable platform. The bar plot reports quantification of the percentage of foot falls ($n=6-8$ mice, two-sided, unpaired Student's *t*-test, $P=0.57$, mean \pm s.e.m.). **d**, Chronophotography of mice performing classic behavioral paradigms in ecological environments while receiving continuous photostimulation of the lumbar spinal cord. The paradigms include climbing up a rope, swimming in a large tank of water and narrow beam walking.

located regions. We addressed this possibility with computer simulations.

We complemented our anatomical model with finite element models of light penetration within the spinal cord (Fig. 3a,b). Simulations predicted that positioning the micro-LEDs above the dorsal horns would result in the most efficient photostimulation of afferent fibers and spinal interneurons (Fig. 3a). Compared with a die positioned over the midline of the spinal cord, this location minimized the impact of light-diffracting, lipid-rich myelin on photon penetration.

Spatially selective targeted photostimulation. We sought to illustrate the relevance of these simulations to steer the configuration of micro-LED arrays that maximize the spatial selectivity of the photostimulation. Specifically, we asked whether the rostrocaudal location of the micro-LEDs was important to target specific motor pools.

We visualized the anatomical location of tibialis anterior motoneurons using intramuscular pseudo-rabies injections (Fig. 3b). Integration of this information into the computational model predicted that micro-LEDs positioned over the dorsal horns of caudal lumbar segments would maximize the photostimulation of neural pathways, leading to the activation of motoneurons innervating tibialis anterior (Fig. 3b–d). We validated these predictions in mice expressing channelrhodopsin (ChR2) in excitatory neurons, including proprioceptive neurons that project directly on to motoneurons (Extended Data Fig. 6). We fabricated a micro-LED array with two channels positioned over the dorsal horns of rostral and caudal lumbar segments. Photostimulation delivered from the LED channel targeting caudal lumbar segments elicited a robust muscle response in tibialis anterior, which provoked a vigorous dorsiflexion of the foot (Fig. 3d, Extended Data Fig. 6 and Supplementary Video 2). The amplitude of muscle responses increased linearly with the intensity of photostimulation (Fig. 3d). In comparison, photostimulation delivered over the rostral lumbar segments elicited responses of smaller amplitude, as expected based on the distant location of the motor neurons innervating this muscle

(Fig. 3d). These weaker responses were not due to a less efficient photostimulation as such, because the same photostimulation elicited a powerful hip flexion triggered by large muscle responses in the iliopsoas muscle, the motoneurons of which are embedded in the illuminated rostral lumbar segments (Extended Data Fig. 6). We reproduced these observations for the medial gastrocnemius muscle (Extended Data Fig. 6).

Photostimulation over the entire spectrum of light. The rapidly evolving library of experimental opsins offers a broad repertoire of tools to target cellular mechanisms^{23,24}. These opsins are activated by specific wavelengths spanning the entire spectrum of light. To be able to target any opsin with our micro-LED array, we integrated a silicone–phosphor composite coating over the micro-LED, which down-converted the emitted blue light toward the desired wavelengths without compromising the overall biointegration of the micro-LED array (Fig. 1b and Extended Data Fig. 2b).

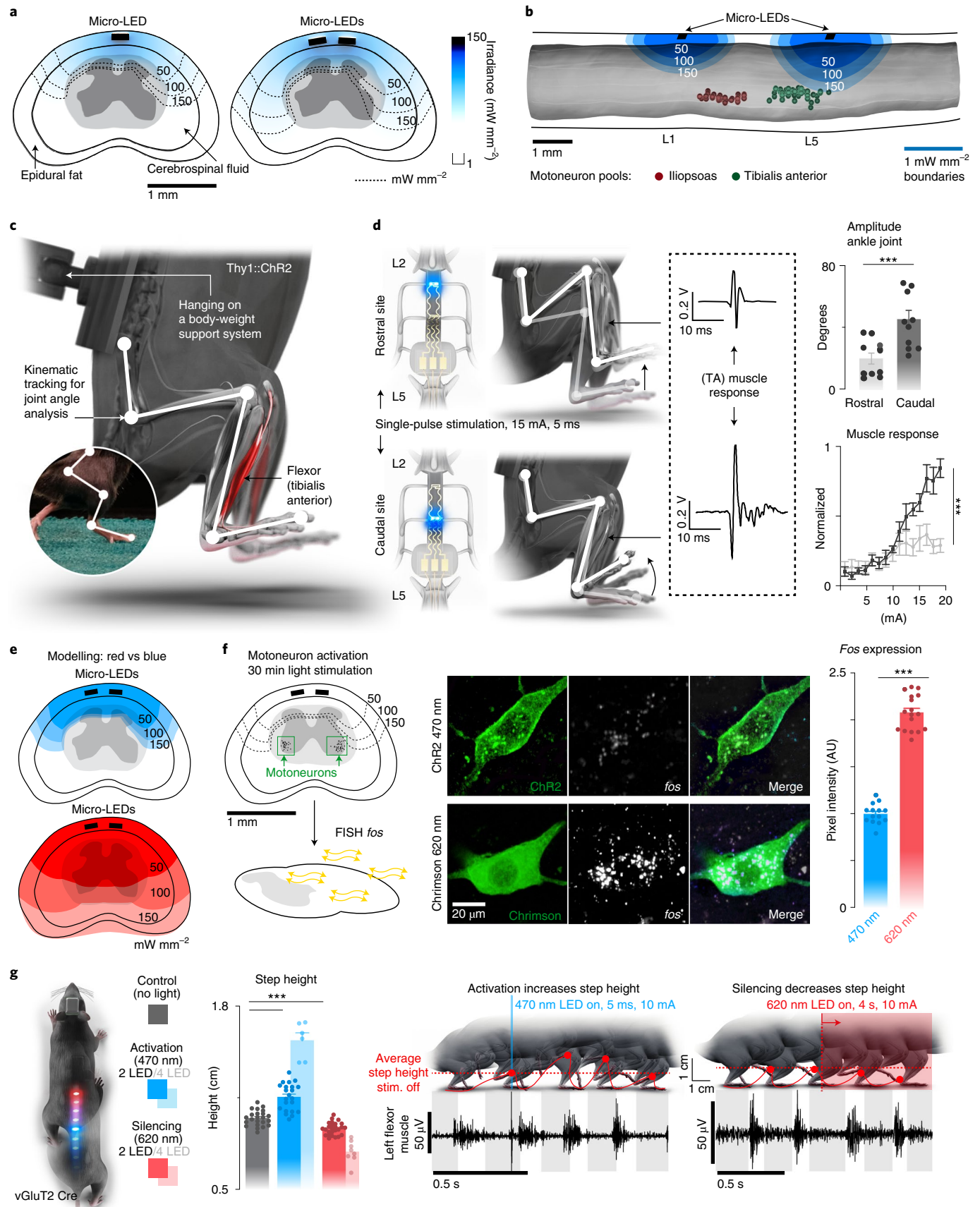
We asked whether our micro-LED array could activate the red-shifted (590-nm) ChrimsonR opsins²⁵ from interneurons located in the intermediate lamina. We expressed these opsins in vGluT2^{ON} neurons using targeted injections of AAV-syn-flex-ChrimsonR-tdTomato in the spinal cord of vGluT2-cre mice (Extended Data Fig. 7). Activation of red-shifted LED channels positioned over the rostral or caudal lumbar segments elicited robust muscle responses that produced extensive movements of the hip or ankle, respectively (Extended Data Fig. 7 and Supplementary Video 2). This spatial specificity mirrored the anatomical location of motoneurons innervating hip flexor muscles versus ankle flexor muscles (Fig. 3b).

Simulations predicted that red-shifted light could penetrate the entire depth of the spinal cord, whereas blue light extinguished rapidly when entering these tissues (Fig. 3e). Therefore, we asked whether red-shifted light could be allowed to target poorly accessible motoneurons, which are nested in the deepest lamina of the ventral spinal cord. To test this prediction, we used intersectional genetics to express red-shifted or blue-activated opsins in sparse populations of motoneurons (Fig. 3f). Although the limited number

Fig. 3 | Targeted photostimulation across the entire spinal cord. **a**, Simulations showing the penetration of blue light depending on the location of the micro-LED along the mediolateral direction. **b**, Simulations predicting the optimal rostrocaudal location of the micro-LED to target activation to tibialis anterior and iliopsoas motoneurons, the location of which was identified with intramuscular rabies injections. **c**, Experimental setup to measure leg kinematics and muscle responses after targeted photostimulation of the lumbar spinal cord in Thy1-ChR2 mice. **d**, Reconstructed leg movements and muscle responses after one-pulse photostimulation delivered over the rostral versus the caudal lumbar spinal cord. The bar plot reports the range of motion induced by the photostimulation ($n=10$ mice, two-sided, unpaired Student's *t*-test, $***P=0.0021$, mean \pm s.e.m.). The plot reports the area under the curve of rectified muscle responses after photostimulation ($n=5$ mice; ANOVA, $***P<0.0001$, mean \pm s.e.m.). TA, tibialis anterior. **e**, Simulations reporting the attenuation of blue- (470 nm) versus red-shifted (620 nm) photostimulation through spinal tissues. **f**, Photographs showing the expression of the immediate early gene *fos* in motoneurons expression ChR2 or Chrimson after blue- (470 nm) versus red-shifted (620 nm) photostimulation. Bar plots report the relative expression of *fos* mRNA after blue- (470 nm) versus red-shifted (620 nm) photostimulation ($n=14/17$ motoneurons for 470-nm/620-nm stimulation; $n=3$ mice per group; two-sided, unpaired Student's *t*-test, $***P<0.0001$, mean \pm s.e.m.). AU, arbitrary units. **g**, Mice expressing ChR2 (470 nm) and Jaws (600 nm) in vGluT2^{ON} neurons stepping on a treadmill while receiving pulses of blue- (470 nm, 2 LEDs) versus red-shifted (620 nm, 2 LEDs) photostimulation. Reconstructions of leg movements include foot trajectories and concomitant activity of tibialis anterior; shaded and empty boxes correspond to stance and swing phases, respectively. Bar graph reporting the step height for each condition ($n>30$ steps per condition, $n=2$ mice for 2 LEDs at 470 nm, $n=6$ mice for 4 LEDs at 470 nm, $n=2$ mice for 2 LEDs at 620 nm and $n=8$ mice for 4 LEDs at 620 nm; one-way ANOVA, $***P<0.0001$, mean \pm s.e.m.). Shaded bars represent mice that expressed a single opsin over the entire lumbar spinal cord and were activated with four LEDs.

of targeted motoneurons was insufficient to elicit muscle contractions, the robust expression of the immediate early gene *Fos* in motoneurons revealed the sustained activation of these cells after

30 min of photostimulation with red-shifted light (Fig. 3f). In contrast, blue light failed to recruit motoneurons, thus confirming the predictions of the computational model (Fig. 3e).



This technology opened the possibility of achieving two-color optogenetic activation and inhibition of targeted cell populations, which we tested in mice coexpressing ChR2 (470 nm) and Jaws²⁶ (600 nm) in vGlut2^{ON} neurons (Fig. 3g and Extended Data Fig. 7). We prepared a micro-LED array with two spectrally distinct light emission channels at two spatially distinct rostrocaudal positions. In the same mouse, blue-light activation of vGlut2^{ON} neurons elicited strong muscle responses, whereas inhibition of vGlut2^{ON} neurons with red-shifted light reduced the vigor of locomotor movements ($n = 3$ mice; Fig. 3g).

Guideline for efficient and safe spinal cord photostimulation.

The reliable activation of opsins such as Jaws that drive hyperpolarization in neurons requires the delivery of sustained photostimulation. Duty cycles with extended stimulation ON times can lead to tissue heating, which alters neuronal responses²⁰. We assessed these thermal constraints comprehensively.

We performed simulations to predict the diffusion of heat in the spinal cord depending on the irradiance and duty cycle of photostimulation (Fig. 4a). Second, we measured the temperature directly within the posterior gray column of the spinal cord across the functional range of current intensities (Fig. 4b, Extended Data Fig. 8 and Supplementary Video 3). These simulations and measurements identified time windows and temporal delays between experiments to avoid alterations of neuronal responses and tissue damage.

To confirm these findings, we continuously illuminated the spinal cord of opsin-free mice with light of increasing intensity while the animals were stepping on a treadmill. To avoid interference from volitional modifications of leg movements, we conducted these experiments in mice with complete spinal cord injury. We activated lumbar locomotor centers below the injury with a serotonergic pharmacotherapy that enabled automated stepping without any contribution by the brain²⁷. Clear locomotor deficits emerged during photostimulation. The extent of these deficits augmented with increasing time and radiant intensity (Fig. 4c and Supplementary Video 3).

These results establish a guideline for light-delivery parameters that enable reliable interrogation of spinal circuits in mice.

Ultrafast closed-loop control of photostimulation. We next sought to illustrate the capabilities of our optoelectronic system for closed-loop photostimulation. We implemented a paradigm typically used in behavioral experiments and neuroprosthetic applications, wherein the onset of a burst of muscle activity instantly triggers photostimulation²⁸. We conducted this experiment in Thyl-ChR2 mice, which were implanted with a micro-LED array targeting lumbar segments (Supplementary Video 4).

We interfaced four pairs of thin wires and one reference (ground) wire with the wearable platform to acquire differential recordings of electromyographic (EMG) activity from chronically implanted leg muscles. EMG signals were sampled at 8 kSs^{-1} (per channel) with an analog bandwidth of 3.2 kHz (Fig. 5a,b). The signals were then conditioned on-chip to remove mains interference, apply a band-pass filter ($100\text{--}1,000\text{ Hz}$) and down-sample to 2 kSs^{-1} . The processed signals were displayed in real time on the tablet while the

mouse was walking freely along a straight corridor without any constraint (Fig. 5d). The parameters for closed-loop photostimulation were configured on the tablet, but the control algorithm ran on the wearable platform. On-chip operations enabled closed-loop photostimulation with latencies as low as 15 ms (Extended Data Fig. 3). The control algorithm automatically delivered a brief single pulse of photostimulation (10 ms) each time a new burst of EMG activity was detected in the tibialis anterior muscle (Fig. 5c). Ultrafast EMG-triggered photostimulation induced a systematic and reproducible reduction of step length without impeding the continuous progression of the mice (Fig. 5d and Supplementary Video 4).

Contribution of specific neurons and pathways to movement.

We finally deployed a series of in vivo experiments to demonstrate the unprecedented versatility of our wireless optoelectronic system in interrogating key components of the locomotor circuitry in ecological environments or after neurological injury.

We asked whether the optoelectronic system could modulate descending pathways, even if the axons were confined to poorly accessible regions of the white matter. We used intersectional genetics to express Jaws along the entire extent of axons originating from neurons of the reticular formation that establish synapses within the lumbar gray matter (Extended Data Fig. 9). These axons extend in the poorly accessible lateral and ventral columns of the white matter, and terminate into ventral regions of the spinal cord. The reticular formation contributes to the production of locomotion and regulation of posture^{22,29}. Sudden silencing of reticulospinal fibers during unconstrained locomotion arrested leg movements. This interruption lasted as long as the photostimulation was turned on (Fig. 6b,c and Supplementary Video 5). This result was unexpected, because such deficits were not detected when we silenced reticulospinal neurons using chemogenetics, which is a comparatively slow-acting method²². Therefore, we sought to replicate these observations when silencing the corticospinal tract (Fig. 6d and Extended Data Fig. 9). Previous studies showed that chemogenetic silencing²² or ablation³⁰ of this pathway does not affect basic walking²⁹. We found that the silencing of corticospinal tract fibers in the lumbar spinal cord during basic walking induced moderate paw dragging and trunk instability (Fig. 6e, Extended Data Fig. 9 and Supplementary Video 5). These deficits resonate with the expected role of the corticospinal tract during walking in humans³¹. Together, these results emphasized the importance of fast perturbation dynamics for interrogating neural circuits.

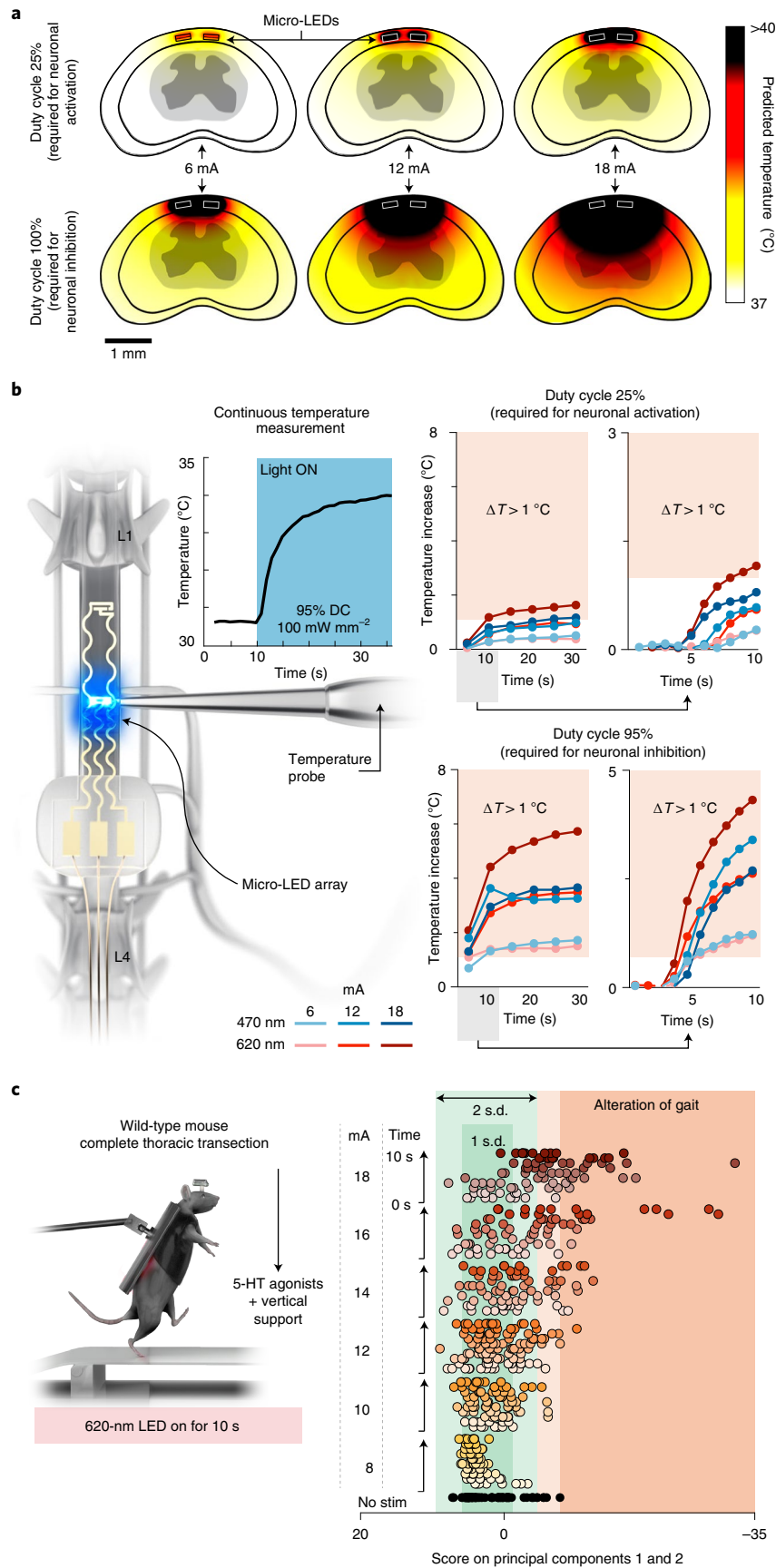
We next aimed to demonstrate the ability of our optoelectronic system to manipulate deeply located interneurons in ecological conditions. We expressed ChrimsonR or Jaws into Vsx2-expressing interneurons (Extended Data Fig. 10), which are involved in left-right alternation and locomotor vigor³². The sudden activation or inhibition of Vsx2-expressing interneurons during unconstrained swimming disrupted interlimb coordination (Fig. 6f–h and Supplementary Video 5).

Sensory feedback pathways are essential components of the circuits that produce locomotion, in particular after injury³³. To illustrate the ability of the optoelectronic system to modulate these pathways, we expressed Jaws in proprioceptive neurons located in the dorsal root ganglia of mice with complete spinal cord injury

Fig. 4 | Guideline for effective yet safe spinal cord photostimulation. **a**, Simulation of heat diffusion in spinal cord tissue with photostimulation protocols eliciting activation of ChR2 (25% duty cycle) or Jaws (95% duty cycle). **b**, In vivo measurement of heat using a temperature probe inserted in the dorsal horn during photostimulation, with the settings necessary to target ChR2 (top: 25% duty cycle, wavelength 470 nm, two LEDs) or Jaws (bottom: 95% duty cycle, wavelength 620 nm, two LEDs). The plots (and zoom-in windows) report the changes in temperature over time for three levels of intensity. **c**, Wild-type mice with complete spinal cord injury stepping on a treadmill after the reactivation of the lumbar spinal cord with serotonergic agonists. The spinal cord is illuminated for 10 s, at various intensities. Kinematic recordings are converted into a series of gait feature quantifications that are submitted to a principal component analysis. Locomotor performance is evaluated as the score on principal components 1 and 2. The plot reports the changes in locomotor performance over time for each tested photostimulation intensity ($n = 3$ mice).

(Extended Data Fig. 10). All the paralyzed mice exhibited robust locomotion in response to the serotonergic pharmacotherapy. Sudden silencing of proprioceptive feedback circuits mediated

an unexpected augmentation in the vigor of locomotor movements, which led to an increase in step height associated with an extended duration of bursts in ankle flexor muscles (Fig. 6k and



Supplementary Video 5). These behavioral responses were transient, because the increase in step height only lasted for six to ten steps before the mice collapsed.

Discussion

We resolved the challenges underlying the conception of a chronic optoelectronic system that enables the safe, long-term, closed-loop photostimulation of any targeted neurons or pathways throughout the mouse spinal cord, under untethered, unrestricted and ecological conditions. We also established a guideline for spinal cord optogenetics in mouse models to conform epidural implants to spinal cord statics and dynamics, optimize LED positioning and avoid tissue heating that alters neuronal responses.

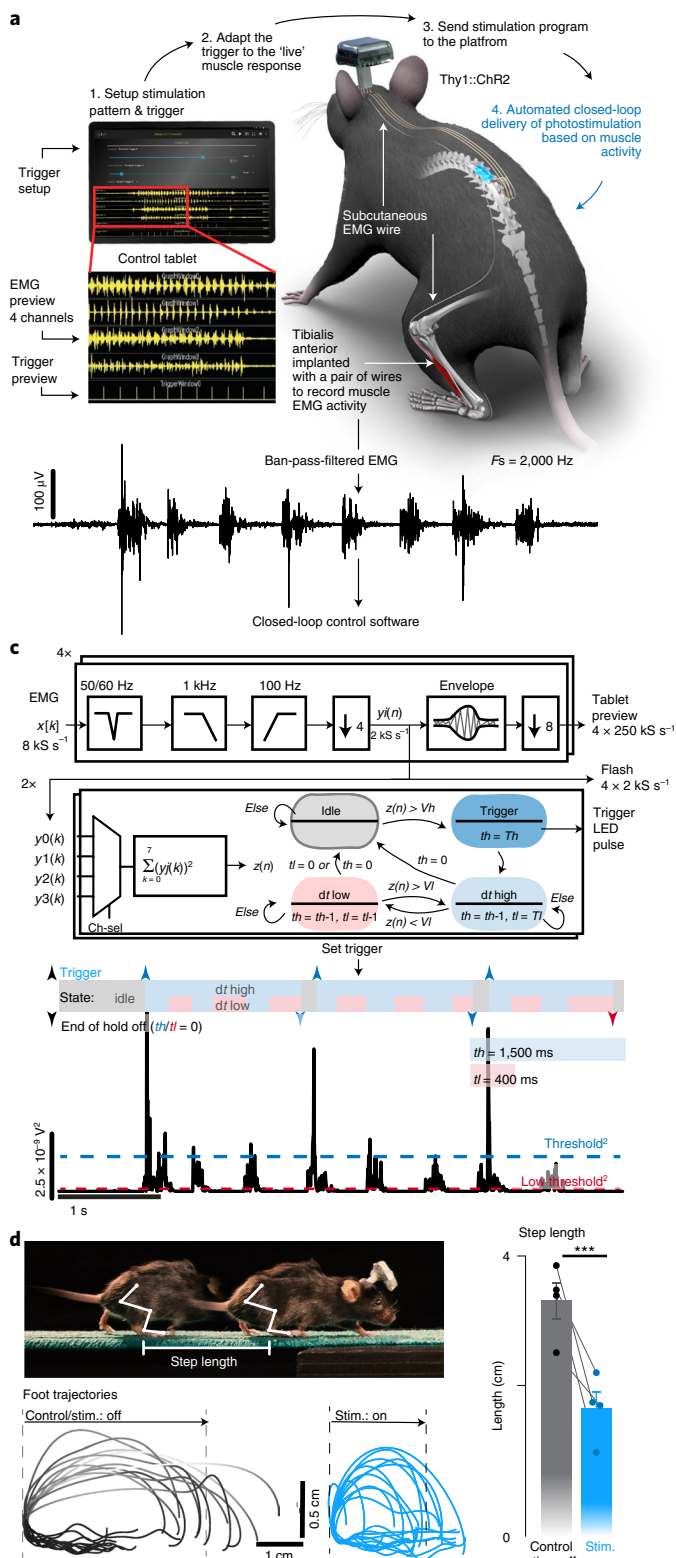
When designing this system, we aimed to include all the desired features of spinal cord optogenetics. We conceived a system wherein a conformable array accommodates tailored configurations of micro-LEDs with customizable emission spectra, allowing concurrent multicolor illuminations of targeted neuronal populations distributed across various locations of the spinal cord, including deep regions. This versatility befits the functional interrogation of any targeted neurons within the dorsal root ganglia or spinal cord, as well as any white matter-embedded axons from any targeted neuronal pathways.

With few exceptions, functional interrogation of spinal pathways has been limited to permanent ablations or slow-acting manipulations, such as chemogenetics³⁴ (minutes to hours) or conditional cell ablations³⁵ (weeks or longer). Our system allowed us to perform a series of experiments that revealed the incompatibility of these timescales with the study of dynamic circuit interactions, which emerge within millisecond windows. For example, we previously showed that chemogenetic silencing of excitatory reticulospinal or cortico-spinal tract neurons had no detectable impact on locomotor control in intact mice²². Instead, we found that the sudden silencing of these descending pathways within lumbar segments led to clear gait deficits, which depended on the specifically targeted pathway. The sudden silencing prevents redundant systems from compensating for the missing inputs, which probably occurs during slow-acting interventions³⁶. It is also possible that the silencing within the spinal cord leads to incongruent commands, especially from cortical neurons that multiplex executive commands through various descending pathways, in addition to direct inputs to the spinal cord. In the same vein, we observed an unexpected increase in the amplitude of locomotor movements when silencing proprioceptive feedback circuits.

This counterintuitive response could not be predicted from previous genetic ablation experiments of proprioceptive afferents that reported sustained gait deficits after the loss of proprioception^{33,37}. Although the mechanisms underlying these transient responses require further investigation, our results stress the importance of fast perturbation dynamics to interrogate the function of spinal circuits involved in the production of motor behaviors.

Fig. 5 | Ultrafast closed-loop control of photostimulation to alter movement.

a, Wireless closed-loop optoelectronic system, including recordings of EMG signals from pair of wires chronically implanted into selected muscles and photostimulation. A tablet displays the signals and photostimulation events in real time, and allows configuration of the algorithms for closed-loop operations. **b**, Conditioned (bandpass filter, mains interference suppression, down-sampling) recording of tibialis anterior activity. **c**, Signal conditioning and flow chart of the closed-loop algorithm to determine the timing of photostimulation: the sum of the square values of eight consecutive samples (2 kS s^{-1}) is taken as a short-term signal power measure $z[n]$. A stimulation is triggered for $z[n] > V_h$, then a timer set to th ensures that there is no further stimulation event for th ms—except, if the signal power $z[n]$ falls for longer than tl under V_l . Signal power measures $z[n]$ and algorithm state for given threshold and hold-off times. **d**, Thy1-ChR2 mouse walking freely while a single-pulse (10 ms) of blue light (470 nm, two LEDs) is delivered over lumbar segments each time a burst of EMG activity is detected in the tibialis anterior muscle. Successive foot trajectory (toe marker) during walking without and with photostimulation (Stim.). Bar graph reporting the step length for both conditions ($n = 4$ mice, two-sided, paired Student's t -test, $***P < 0.0207$, mean \pm s.e.m.).



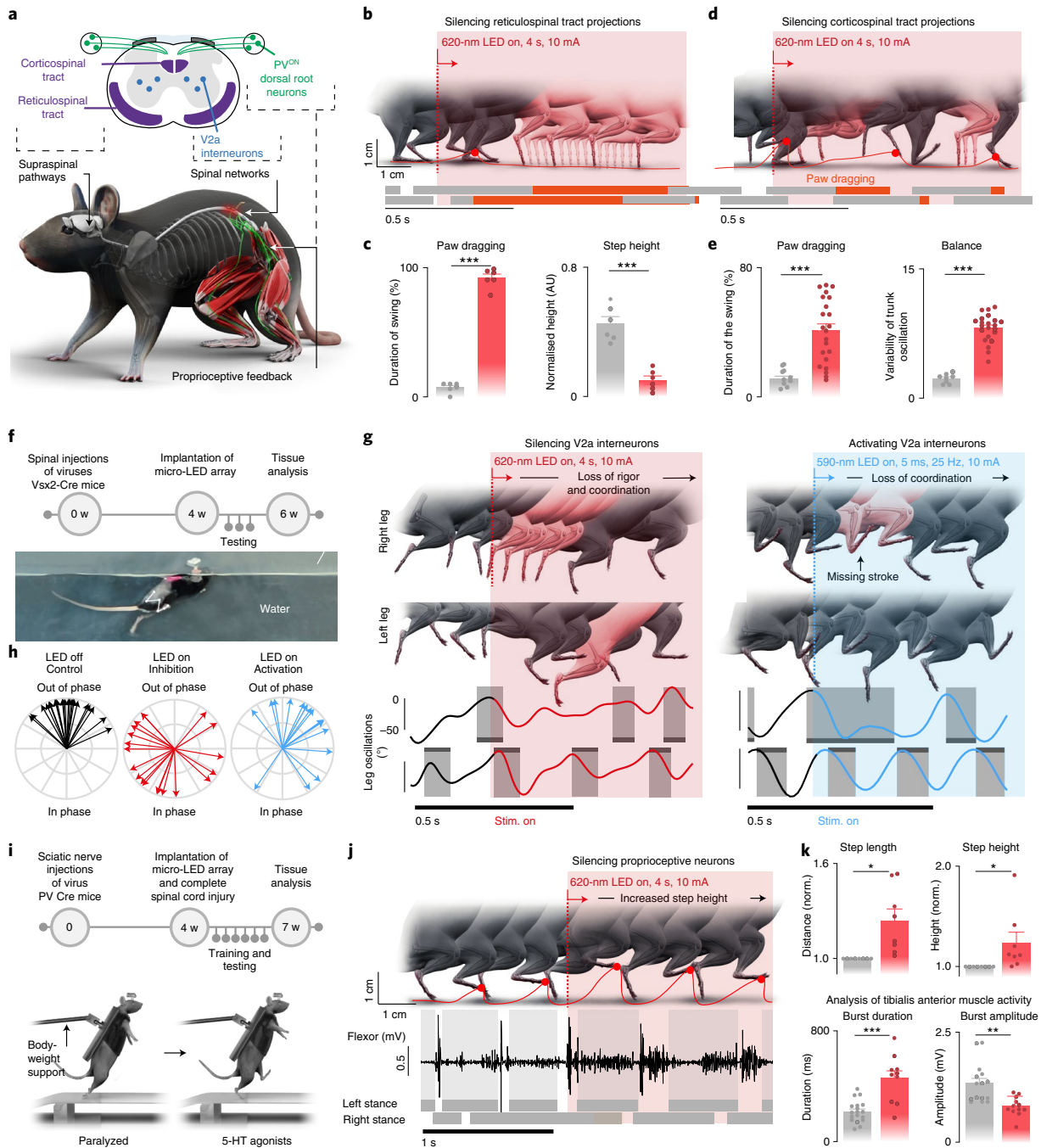


Fig. 6 | Contribution of specific neurons and pathways to movement. **a**, Schematic showing the anatomical location of neurons and neural pathways that we targeted using intersectional genetics. **b**, Reconstructed sequence of leg kinematics during walking while a red-shifted light (four LEDs) is delivered over the spinal cord to silence reticulospinal tract projections. The occurrence of stance phases and paw dragging events is displayed for both legs below leg kinematics. **c**, Bar plots reporting gait parameters most affected by the silencing of reticulospinal fibers ($n=3$ mice; two-sided, unpaired Student's t -test, $***P < 0.0001$, mean \pm s.e.m.). AU, arbitrary units. **d**, Reconstructed sequence of leg kinematics during walking while delivering a red-shifted light (four LEDs) over the spinal cord to silence corticospinal tract projections. The occurrence of stance phases and paw-dragging events is displayed for both legs below leg kinematics. **e**, Bar plots reporting gait parameters most affected by the silencing of corticospinal tract fibers ($n=3$ mice; two-sided, unpaired Student's t -test, $***P < 0.0001$, mean \pm s.e.m.). **f**, Timeline of experiments for targeted expression of *Jaws* (inhibition) or *Chrimson* (activation) in V2a interneurons (w indicates weeks). The photograph shows kinematic recordings during swimming along a water corridor. **g**, Reconstructed sequence of left and right leg kinematics during swimming are shown together with the oscillations of both legs. Gray shaded areas indicate the occurrence of a stroke. V2a interneurons were silenced or activated with sudden photostimulation over the lumbar spinal cord (620 nm/590 nm, four LEDs). **h**, Polar plot reporting the coordination between left and right strokes during swimming under the different experimental conditions ($n=3$ mice). **i**, Timeline of experiments for targeted expression of *Jaw* in PV^{ON} neurons of the dorsal root ganglia in mice. **j**, Reconstructed sequence of leg kinematics during stepping together with EMG activity of the tibialis anterior muscle while suddenly delivering a red-shifted light (four LEDs) delivered over the spinal cord to silence proprioceptive neurons. **k**, Bar plots reporting the step length, step height and features of tibialis anterior EMG activity ($n=3$ mice; two-sided unpaired Student's t -test, $*P < 0.05$, $**P < 0.01$, $***P < 0.001$, mean \pm s.e.m.).

Clinical trials have started assessing the safe use of opsins for treating neurological deficits in patients³⁸. As the spinal cord is a primary target of optogenetic-based therapies, clinical optogenetics will trigger a surge of interest in medical devices capable of illuminating the spinal cord². In this respect, our wireless optoelectronic system obeys the key principles underlying the ecological design of medical devices³⁹, thus opening a pathway to develop systems for the human spinal cord.

Online content

Any methods, additional references, Nature Research reporting summaries, source data, extended data, supplementary information, acknowledgements, peer review information; details of author contributions and competing interests; and statements of data and code availability are available at <https://doi.org/10.1038/s41587-021-01019-x>.

Received: 19 October 2020; Accepted: 14 July 2021;

Published online: 27 September 2021

References

- Deisseroth, K. Optogenetics. *Nat. Methods* **8**, 26–29 (2011).
- Won, S. M., Song, E., Reeder, J. T. & Rogers, J. A. Emerging modalities and implantable technologies for neuromodulation. *Cell* **181**, 1–21 (2020).
- Roy, A. et al. Optogenetic spatial and temporal control of cortical circuits on a columnar scale. *J. Neurophysiol.* **115**, 1043–1062 (2016).
- Jeong, J. W. et al. Wireless optofluidic systems for programmable in vivo pharmacology and optogenetics. *Cell* **162**, 662–674 (2015).
- Kim, T. II et al. Injectable, cellular-scale optoelectronics with applications for wireless optogenetics. *Science* **340**, 211–216 (2013).
- Montgomery, K. L. et al. Wirelessly powered, fully internal optogenetics for brain, spinal and peripheral circuits in mice. *Nat. Methods* **12**, 3–5 (2015).
- Qazi, R. et al. Wireless optofluidic brain probes for chronic neuropharmacology and photostimulation. *Nat. Biomed. Eng.* **3**, 655–669 (2019).
- Shin, G. et al. Flexible near-field wireless optoelectronics as subdermal implants for broad applications in optogenetics. *Neuron* **93**, 509–521.e3 (2017).
- Montgomery, K. L., Iyer, S. M., Christensen, A. J., Deisseroth, K. & Delp, S. L. Beyond the brain: optogenetic control in the spinal cord and peripheral nervous system. *Sci. Transl. Med.* **8**, 337rv5–337rv5 (2016).
- Gutruf, P. & Rogers, J. A. Implantable, wireless device platforms for neuroscience research. *Curr. Opin. Neurobiol.* **50**, 42–49 (2018).
- Xue, Y. et al. A wireless closed-loop system for optogenetic peripheral neuromodulation. *Nature* **565**, 361–365 (2018).
- Michoud, F. et al. Epineural optogenetic activation of nociceptors initiates and amplifies inflammation. *Nat. Biotechnol.* **39**, 179–185 (2020).
- Caggiano, V., Sur, M. & Bizzi, E. Rostro-caudal inhibition of hindlimb movements in the spinal cord of mice. *PLoS ONE* **9**, 100865 (2014).
- Lu, C. et al. Flexible and stretchable nanowire-coated fibers for optoelectronic probing of spinal cord circuits. *Sci. Adv.* **3**, e1600955 (2017).
- Park, S. II et al. Soft, stretchable, fully implantable miniaturized optoelectronic systems for wireless optogenetics. *Nat. Biotechnol.* **33**, 1280–1286 (2015).
- Samineni, V. K. et al. Fully implantable, battery-free wireless optoelectronic devices for spinal optogenetics. *Pain* **158**, 2108–2116 (2017).
- Wang, Y. et al. Flexible and fully implantable upconversion device for wireless optogenetic stimulation of the spinal cord in behaving animals. *Nanoscale* **12**, 2406–2414 (2020).
- Mineev, I. R. et al. Electronic dura mater for long-term multimodal neural interfaces. *Science* **347**, 159–163 (2015).
- Mondello, S. E. et al. Optogenetic surface stimulation of the rat cervical spinal cord. *J. Neurophysiol.* **120**, 795–811 (2018).
- Owen, S. F., Liu, M. H. & Kreitzer, A. C. Thermal constraints on in vivo optogenetic manipulations. *Nat. Neurosci.* **22**, 1061–1065 (2019).
- Schönle, P. et al. A multi-sensor and parallel processing SoC for miniaturized medical instrumentation. *IEEE J. Solid-State Circuits* **53**, 2076–2087 (2018).
- Asboth, L. et al. Cortico-reticulo-spinal circuit reorganization enables functional recovery after severe spinal cord contusion. *Nat. Neurosci.* **21**, 576–588 (2018).
- Deisseroth, K. Optogenetics: 10 years of microbial opsins in neuroscience. *Nat. Neurosci.* **18**, 1213–1225 (2015).
- Zhang, F. et al. The microbial opsin family of optogenetic tools. *Cell* **147**, 1446–1457 (2011).
- Klapoetke, N. C. et al. Independent optical excitation of distinct neural populations. *Nat. Methods* **11**, 338–346 (2014).
- Chuong, A. S. et al. Noninvasive optical inhibition with a red-shifted microbial rhodopsin. *Nat. Neurosci.* **17**, 1123–1129 (2014).
- Courtine, G. et al. Transformation of nonfunctional spinal circuits into functional states after the loss of brain input. *Nat. Neurosci.* **12**, 1333–1342 (2009).
- Wenger, N. et al. Spatiotemporal neuromodulation therapies engaging muscle synergies improve motor control after spinal cord injury. *Nat. Med.* **22**, 5–7 (2016).
- Kiehn, O. & Dougherty, K. Locomotion: circuits and physiology. in *Neuroscience in the 21st Century: From Basic to Clinical* 1209–1236 (Springer New York, 2013). https://doi.org/10.1007/978-1-4614-1997-6_42
- Bieler, L. et al. Motor deficits following dorsal corticospinal tract transection in rats: voluntary versus skilled locomotion readouts. *Heliyon* **4**, e00540 (2018).
- Barthélemy, D., Grey, M. J., Nielsen, J. B. & Bouyer, L. Involvement of the corticospinal tract in the control of human gait. *Progr. Brain Res.* **192**, 181–197 (2011).
- Crone, S. A., Zhong, G., Harris-Warrick, R. & Sharma, K. In mice lacking V2a interneurons, gait depends on speed of locomotion. *J. Neurosci.* **29**, 7098–7109 (2009).
- Takeoka, A., Vollenweider, I., Courtine, G. & Arber, S. Muscle spindle feedback directs locomotor recovery and circuit reorganization after spinal cord injury. *Cell* **159**, 1626–1639 (2014).
- Roth, B. L. DREADDs for neuroscientists. *Neuron* **89**, 683–694 (2016).
- Ruedl, C. & Jung, S. DTR-mediated conditional cell ablation—progress and challenges. *Eur. J. Immunol.* **48**, 1114–1119 (2018).
- Yizhar, O., Fenno, L. E., Davidson, T. J., Mogri, M. & Deisseroth, K. Optogenetics in neural systems. *Neuron* **71**, 9–34 (2011).
- Takeoka, A. & Arber, S. Functional local proprioceptive feedback circuits initiate and maintain locomotor recovery after spinal cord injury. *Cell Rep.* **27**, 71–85.e3 (2019).
- Yun, S. H. & Kwok, S. J. J. Light in diagnosis, therapy and surgery. *Nat. Biomed. Eng.* **1**, 0008 (2017).
- Courtine, G. & Bloch, J. Defining ecological strategies in neuroprosthetics. *Neuron* **86**, 29–33 (2015).

Publisher's note Springer Nature remains neutral with regard to jurisdictional claims in published maps and institutional affiliations.

© The Author(s), under exclusive licence to Springer Nature America, Inc. 2021

Methods

Micro-LED array fabrication. The fabrication of the micro-LED array is illustrated in Extended Data Fig. 2a. The fabrication started with the spin-coating of a 2.4- μm -thick layer of poly(imide) (HD Microsystems GmbH, catalog no. PI2610) on a 4-inch silicon wafer coated with Ti/Al layers (5/100 nm). After curing of the poly(imide) (2 h at 300 °C in an N_2 oven), a Ti/Au/Ti film (5/250/5 nm) was sputtered after O_2 plasma surface activation (Alliance Concept, catalog no. AC450). Photolithography (MicroChemicals, catalog no. AZ1512) and successive wet and reactive-ion etchings (RIEs) patterned the metallization layer. The latter were encapsulated with a second layer of poly(imide) (2- μm thick). The poly(imide)–metal–poly(imide) stack was next patterned with photolithography (MicroChemicals, catalog no. AZ9260) and RIE. Then, a SiO_2 layer (15 nm) was sputtered on the patterned poly(imide) structures, followed by the spin-coating of a 20- μm -thick layer of poly(dimethylsiloxane) (PDMS) (Sylgard 184, Dow Corning). A third photolithography (MicroChemicals, catalog no. AZ40XT) and RIE etching of the PDMS revealed the device shape and defined the micro-LED integration sites. Small bumps of solder paste (~50- μm diameter, Chipquik, catalog no. SMDTLFPI0T5) were manually deposited on the contact pads. Next, micro-LEDs (Cree Inc., catalog no. TR2227) were positioned on to these pads using pick-and-place equipment (JFP Microtechnic). The wafer was then placed on a hotplate at 165 °C to electrically and mechanically bond the micro-LEDs. For hermeticity, a 12 wt% solution of poly(isobutylene) (PIB, Oppanol, BASF) in cyclohexane (Sigma-Aldrich) was drop casted at the die surface via pneumatic printing. To target activation of red-shifted opsins, a PDMS–phosphor composite (50 wt%, PhosphorTech, catalog no. OR02 or R620) was printed over PIB-covered blue micro-LEDs. A final encapsulating layer of PDMS (60- μm -thick) was printed at the surface of the substrate, placing the interconnect's metallization layer in the mechanical neutral plane. The circuit pads were soldered to copper wires (Cooner wires, catalog no. CZ 1103), then sealed with silicone (Dow Corning, catalog no. 734). Finally, the micro-LED array was released from the wafer by anodic dissolution of the Al layer (2-V bias in a NaCl-saturated H_2O solution).

Wireless recording and stimulation platform. We used two versions of the platform. The first version, which did not include recording capabilities, has been described in detail previously¹². The second version was a substantially improved system that included our customized system-on-chip (SoC)²¹. It incorporated the LED driver of the previously used front-end chip, but extended far beyond in functionality. It featured 9 channels for low-voltage (ExG) signal acquisition, 4 current acquisition channels, 32 LED-driving channels, 1 complex impedance measurement channel, 6 electrical neural stimulation channels and a 4 + 1-core MCU. In the wireless unit, the limited pin count of the small head-mounted connector (16-pin connector, Omnetics, catalog no. A79113-001) constrained us to interface only four differential ExGs, one differential current-sensing and two LED-driving channels. The antenna design was revised and is discussed in more detail below. The device further features a 256-MB flash storage device (GigaDevice, catalog no. GD5F4GQ4RCYIG) for long-term recording of raw signals and experimental protocols, and a BLE SoC (Nordic Semiconductor, catalog no. nRF5283) for wireless connection to an Android tablet PC running a dedicated app.

The customized integrated circuit (IC) SoC was fabricated in 130-nm 1P8M CMOS technology with MIM capacitor and SAB resistor options. The 20.8-mm² chip-die was wire-bonded into a 7 × 7-mm² 169-pin ball-grid-array package, and was thus compatible with standard electronics assembly and soldering work flows. The printed circuit board (PCB) was manufactured in a standard industrial technology: 6 copper layers in FR4 with 1.0-mm overall thickness and >75- μm features/clearances/drill. Components were placed manually and soldered in a reflow oven (5 min, 230 °C maximum), one side at a time. The system was powered by a 12- to 35-mA h Li-Ion battery (Guangzhou Markyn Battery Co., Ltd, catalog no. GMB031009/GMB501113). This battery enabled 3.5–11 h of operations in closed-loop mode, assuming an average delivery of two current pulses per second with a duration of 5 ms and an intensity of 15 mA. The headstage can be detached from the mouse and recharged in between experiments. For longevity, the bonds across the PCB, connector and battery were reinforced with epoxy, and the whole device encapsulated in silicone (Dow Corning, catalog no. 730).

Design and fabrication of the antenna. We designed a physically small antenna, which can be produced in a simple standard industrial PCB technology and thus directly integrated into a PCB design. The 3D-microstrip antenna design is illustrated in Extended Data Fig. 3. We started with a $\lambda/4$ antenna folded into a square, which was realized with 0.4-mm microstrip traces on the top and bottom layers and 0.2-mm/0.4-mm through-vias. A row of vias in a defined distance (0.2 mm) from the antenna trace acted as the ground plane in the third dimension. It shielded the antenna from PCB design-specific influences and detuned it reproducibly, enabling an electrically smaller antenna. Antenna impedance was matched with a π network to the radiofrequency IC, the exact values for which were found in a series of return loss (S11) measurements and completed with antenna gain measurements in the anechoic chamber. Antenna radiation characteristic measurements are reported in Fig. 1g.

Animal models. Experiments were conducted on adult male or female C57BL/6 mice (body weight 18–35 g, age 8–25 weeks). Thy1-ChR2 (Jackson Laboratory, catalog no. 12350), vGluT2 Cre (Jackson Laboratory, catalog no. 016963), Parvalbumin Cre (Jackson Laboratory, catalog no. 017320) and Vsx2 Cre (MMMRRC 36672, also called Chx10 Cre) transgenic mouse strains were used and maintained on a mixed genetic background (C57BL/6). Housing, surgery, behavioral experiments and euthanasia were performed in compliance with the Swiss Veterinary Law guidelines. Animal care, including bladder voiding, was performed twice daily at the time of the experiment. All procedures were approved by the Veterinary Office of the Canton of Geneva.

Viruses and virus production. Viruses used in the present study were either acquired commercially or produced locally. The following plasmids were used and detailed sequence information is available as detailed or on request: AAV-Dj-hSyn Flex mGFP 2A Synaptophysin mRuby (Stanford Vector Core Facility, reference AAV DJ GVVC-AAV-100, titer 1.15×10^{14} GC ml⁻¹), AAV pmSyn1-EBFP-Cre (Addgene Plasmid, catalog no. 51507), AAV-Syn-FLEX-ChrimsonR-tT (Addgene, catalog no. 62723), AAV-CAG-FLEX-Jaws-KGC-GFP-ER2 (Addgene, catalog no. 84445) and AAV-EF1a-double floxed hChR2(H134R)-mCherry (Addgene, catalog no. 20297). All flexed adeno-associated virus (AAV) vectors used in the present study showed transgene expression only on Cre-mediated recombination. Pseudo-rabies tracing was completed using Bartha strain PRV152 (expressing green fluorescent protein (GFP): 4.9×10^9 plaque-forming units ml⁻¹, Princeton University). The injection volumes, coordinates and experimental purpose are described below.

Surgical procedures. General surgical procedures have been described previously in detail¹². Surgery was performed under aseptic conditions and under 1–2% isoflurane in a flow of oxygen, as general anesthesia, of 0.5–1.0 l min⁻¹. After the surgery, the mice were allowed to wake up in an incubator. Analgesia, buprenorphine (Essex Chemie AG, 0.01–0.05 mg kg⁻¹ subcutaneously) or carprofen (Rimadyl, 5 mg kg⁻¹) was given twice daily for 2–3 d after surgery.

Implantation of the micro-LED array. The interlaminar spaces between vertebrae T12–T13 and L2–L3 were dissected to expose the exit and entry points, respectively, for the implant. A 6/0 Ethilon suture (Ethicon EMEA, catalog no. MPE697H) was passed through the epidural space from T12–T13 to L2–L3, then through the silicone loop of the implant and back through the epidural space. The implant was slid over the spinal cord by gently pulling both ends of the suture rostrally. The connector of the implant was fixed by suturing paraspinous muscles across the connector. The percutaneous connector (16-pin connector, Omnetics Connector Corporation, catalog no. A79112-001) and wires were routed subcutaneously to the head. Three screws (PN: AMS120/5B-25, Antrin miniature specialties) were inserted into the skull, surrounding the percutaneous connector. Fresh dental cement was then poured around the screws and connector, and held in place until cured. The wireless recording and stimulation platform could easily be attached to and detached from this connector during behavioral experiments.

Spinal injections. For lumbar cord injections, the interlaminar spaces between T13–L1 and L1–L2 were dissected. Injections were performed using a pulled-glass pipette driven with the nanoliter pump (Nanoliter 2010 injector, World Precision Instruments) fixed to a stereotaxic frame. Two injections were made on either side of the spinal cord per interlaminar space; 50 nl, at a rate of 100 nl s⁻¹, was injected at 0.6 mm and 0.3 mm below the dorsal surface of the spinal cord.

Brain injections. An incision was made across the skull. For targeting corticospinal neurons in layer V of the motor cortex, Bregma was identified and a craniotomy 1–2 mm medial and –0.5 mm to 2 mm rostrocaudally was performed with a handheld drill. Then 100-nl injections at 3 nl s⁻¹ were made bilaterally at the mediolateral 1.2 mm and 1.7 mm, rostrocaudally at 0 mm, –0.5 mm, –1 mm and –1.5 mm, and dorsoventrally at a depth of 0.5 mm from the brain surface. For targeting descending neurons in the reticulospinal formation, Bregma was identified and a craniotomy 5–6 mm dorsal and 0–2 mm lateral to Bregma was performed. Injections, 100 nl, at 3 nl s⁻¹, were made bilaterally at the mediolateral 0.3 mm, rostrocaudally at –5.8 mm and –6.2 mm, and dorsoventrally at a depth of 5.6 mm from the brain surface.

Muscle and sciatic nerve injections. An incision was made in the skin above the belly of the muscle of interest; 3.5 μl of virus was injected in total per muscle using a 10- μl Hamilton injection syringe. For sciatic nerve injections, an incision was made above biceps femoris. The muscles overlying the sciatic nerve were bluntly dissected until the nerve was exposed. Then, 2 μl of virus was injected into the nerve with a 10- μl Hamilton syringe.

Intersectional virus-targeting strategies. For targeting transgene expression to motor neurons, an rAAV pmSyn1-EBFP-Cre was injected into the sciatic nerve and an AAV5 Syn-FLEX-ChrimsonR-ttT or AAV5 EF1a-double floxed-hChR2(H134R)-mCherry into the lumbar spinal cord. For targeting vGluT2 interneurons in the spinal cord, an AAV5 CAG-FLEX-Jaws-KGC-GFP-ER2 and/or

AAV5 Syn-FLEX-ChrimsonR-tdT was injected into the lumbar spinal cord. For targeting the reticulospinal or corticospinal tract, an AAV5 pmSyn1-EBFP-Cre was injected into the reticular formation or layer V motor cortex, combined with a rAAV CAG-FLEX-Jaws-KGC-GFP-ER2. For targeting V2a interneurons, an AAV5 CAG-FLEX-Jaws-KGC-GFP-ER2 or AAV5 Syn-FLEX-ChrimsonR-tdT was injected into the lumbar spinal cord.

EMG implantation. An incision over the muscle of interest (tibialis anterior, gastrocnemius) was made and, if needed, the muscle was exposed by blunt dissection of overlying tissue. Bipolar intramuscular electrodes were inserted into the muscle parallel to the muscle fiber orientation. To confirm optimal placing, the wires were electrically stimulated, resulting in a muscle. Electrodes were fixed in place by suturing either side of the electrode that exited the muscle⁴⁰. A grounding wire was implanted subcutaneously. Wires were connected to a percutaneous connector (Omnetics Connector Corporation) cemented to the skull.

In vivo temperature measurement. The skin was incised over the thoracic and lumbar spinal cord. A laminectomy at the vertebral level T13 and L1 was performed. A suture was passed from the L2–L3 intralaminar space to the exposed spinal cord. The suture was passed through the loop of the spinal micro-LED array and passed back under the lamina to L2–L3. The implant was placed over the spinal cord with the distal end under L2. The temperature probe (MT-4 thermocouple microprobe, Physitemp Instruments Inc.) was inserted and fixed at L1. The spinal cord was photostimulated at 6, 12 and 18 mA at increasing duty cycles (5–100%; intervals of 5%) for 30 s at a time. We continuously recorded the temperature in the spinal cord.

Algorithm for closed-loop application. The four EMG signals $xi[k]$ were acquired with 3.2 kHz of analog bandwidth at 8 kSs^{-1} . They were then conditioned (mains interference and bandpass filtering) and down-sampled to 2 kSs^{-1} , $yi[n]$, on-chip by MCU software. The $yi[n]$ signals were stored to the on-device flash memory and were further processed for both the tablet preview (a low sampling rate envelope) and the closed-loop stimulation triggering: the sum of the square values of eight consecutive samples was taken as a short-term signal power measure $z[m]$. The user can set (via the tablet–user interface) various parameters: a higher Vh and lower Vl threshold value and high th and low tl dead times. A stimulation was triggered for $z[m] > Vh$, then a timer set to th ensures that there is no further stimulation event for th seconds—except, if the signal power $z[m]$ fell for longer than tl under Vl . Separate trigger conditions can be set for the two LED-driving channels.

Spinal cord injury model. A laminectomy was made at midthoracic level T7–T8. The spinal cord was completely transected with microscissors. To confirm the completeness of the transection, the cut was re-traced with a 32-G needle. Muscles were sutured over the exposed spinal cord and the skin was sutured.

Training. A week after transection injury, mice were trained daily on a locomotor task. Then 5 min before training, the mice received subcutaneous injections of quipazine (5-hydroxytryptamine-2A/C (5-HT)_{2A/C}, 0.2–0.3 mg kg⁻¹) and intraperitoneal injections of the 5-HT agonist, 8-OH-DPAT (5-HT_{1A/7}, 0.05–0.2 mg kg⁻¹). The dose was adjusted based on locomotor performance. Training was conducted bipedally on a treadmill (9 cm s⁻¹, Robomedica) with adjustable robotic support of body weight for 20 min daily.

Behavioral assessments. The wireless recording and stimulation platform were gently attached to the mouse's head connector before the behavioral experiments. Stimulation paradigms for photostimulation required for neuronal activation consisted of 5-ms pulses at 50 Hz (25% duty cycle) and photostimulation required for neuronal inhibition consisted of 20-ms pulses at 50 Hz (100% duty cycle). All other procedures have been described in detail previously²². Limb motor movements were evaluated while running on a treadmill, on a horizontal ladder or during swimming across a straight pool of water. Bilateral leg kinematics were captured either with the Simi Reality Motion Systems (combining up to four cameras) for markerless tracking with DeepLabCut⁴¹ or with the Vicon Motion Systems (combining twelve infrared cameras) for tracking with reflective markers on the crest, hip, knee, ankle joints and distal toes. The limbs were modeled as an interconnected chain of segments and gait parameters were calculated from these. EMG signals (2 kHz) were amplified ($\times 1,000$), filtered ($\times 100$ – $1,000$ bandwidth, A-M Systems Differential AC Amplifier Model 1700) and digitalized with either the Vicon System or the Powerlab system (AdInstruments). The traces were analyzed offline with LabChart.

Analysis of kinematic data. A total of 78 gait parameters were computed for each gait cycle of each limb. All parameters are reported in Supplementary Table 1. To evaluate differences between time points post-implantation or experimental conditions, as well as to identify the most relevant parameters explaining these differences, we implemented a multistep principal component analysis.

Perfusions. Mice were perfused at the end of the experiments. Mice were deeply anesthetized by an intraperitoneal injection of 0.2 ml sodium pentobarbital

(50 mg ml⁻¹). Mice were transcardially perfused with phosphate-buffered saline (PBS) followed by 4% paraformaldehyde in PBS. Tissue was removed and post-fixed for 24 h in 4% paraformaldehyde before being transferred to PBS or cryoprotected in 30% sucrose in PBS.

Computed tomography. Once perfused, the mouse was placed in a 50-ml Falcon tube. The mouse was then scanned in a micro-CT Quantum GX (Perkin Elmer) with a field of view (FOV) of 25 mm at 90 kV and 80 mA over 360° (angle 0.45°) using the high-resolution 14-min protocol. The projections obtained were then reconstructed at a voxel size of 50 μm or 20 μm using the Quantum GX software. Segmentation was performed with Analyze 12.0 (AnalyzeDirect, Inc.).

Magnetic resonance imaging. The mice were placed in a Falcon tube which was filled with Galden (Fluorochem) to match the tissue magnetic susceptibility and improve magnetic field homogeneity around the cord. Mouse cords were scanned on a 9.4-T MR system (Varian Medical Systems) equipped with 400 mT m⁻¹ gradients, using a 3.5-mm diameter birdcage coil for radiofrequency transmission and reception. High-resolution axial anatomical images were acquired using a fast spin-echo sequence (in-plane resolution: $47 \times 47 \mu\text{m}^2$; FOV: $12 \times 12 \text{ mm}^2$; matrix size: 192×192 zero-filled to 256×256 ; slice thickness: 0.5 mm, 20 slices; echo time: repetition time (TE:TR) = 13:5,000 ms; echo train length: 4; TE_{eff} = 13 ms, 24 averages; scan time = 1 h 36 min).

Computational simulations. An anatomically accurate, 3D finite element model of the mouse spinal cord was generated. First, sagittal sections of the gray and white matter were extracted from an atlas of the spinal cord⁴². Second, these sections were placed and scaled manually to fit the collected MRI data. In turn, the cerebrospinal fluid and epidural fat were first segmented from the same datasets, and then sections were extracted and smoothed. All sections were lofted together to generate 3D volumes (Sim4Life by ZMT). The LEDs were approximated as three-layer rectangular structures consisting of PIB, PDMS and SiC (Cree Inc., catalog no. TR2227). The entire geometry was encapsulated in a cylindrical volume to approximate the surrounding tissues as saline. All volumes were imported into COMSOL and discretized into a tetrahedral mesh with extremely fine element size (COMSOL Multiphysics v.5.3: www.comsol.com; COMSOL AB). Physics-based simulations of the bioheat transfer and light penetration were applied. For the former, the bioheat transfer equations were utilized, for which thermal conductivity, density and heat capacity values were exported from an atlas of such values in Sim4Life (<https://itis.swiss/virtual-population/tissue-properties/database/thermal-conductivity>). Dirichlet boundary conditions were applied at the outermost surface of the saline volume. A heat source was applied at the appropriate layer for each simulation. The light penetration was calculated using Helmholtz equations. Scattering and absorption coefficients were taken from various previous publications^{43–45}. Optical parameters of the model are reported in Supplementary Table 2. Dirichlet boundary conditions were implemented for the optode contacts and the outermost surface of the saline volume. A parametric sweep was applied for the power density of the irradiance with values of 50, 100 and 150 mW mm⁻².

X-ray videography. To collect high-speed X-ray video data, animals were positioned in a $15 \times 5 \times 5.5 \text{ cm}^3$ Plexiglas box oriented perpendicular to the beam of a customized X-ray video system (Philips BV 25, 64 kV, 2 mA). The transparent box allowed continuous observation of the mouse with an infrared video camera to trigger the X-ray acquisition at the right moment. The rays were detected by a flat panel detector (196 Hz, Dexela 1207) and acquired with a frame grabber (Matrox Solios eCL-B). Fifteen trials of 10-s length were acquired per animal. Communication with the detector device, video acquisition and correction of image distortions were carried out using customized software (MATLAB, The MathWorks).

Optical measurements. The optoelectronic devices were laminated on a large photodiode (Thorlabs, catalog no. S170C) and covered with a customized reflective piece. The captured light power was measured using an optical power meter (Thorlabs, catalog no. PM100D). For measurements involving micro-LEDs covered with phosphor-PDMS composite, the converted light ($\lambda = 590$ or 620 nm) and the transmitted blue light ($\lambda = 470 \text{ nm}$) powers were quantified individually using optical filters with cut-off $\lambda = 500 \text{ nm}$ (Thorlabs, catalog nos. FES0500, FEL0500).

Accelerated aging. To assess the long-term functionality of the micro-LED array and the safety of its encapsulation over time, accelerated aging experiments were conducted. The optoelectronic devices were immersed in PBS with a pH of 7.4 (1X, Gibco), and its test tube was sealed with parafilm. Then, the devices were stored in an incubator at 67°C, resulting in a sixfold acceleration compared with the mouse body temperature (37°C). Measurements were carried out at room temperature using a constant current source (Keithley 2400 SourceMeter, $i = 5 \text{ mA}$).

Optoelectronic characterization under stretch. To evaluate the stable functionality of the micro-LED array under mechanical strain, cycling experiments were performed. The devices were mounted on a customized uniaxial stretcher

and stretched to 1.15 of their initial length for 100,000 cycles (1 stretching cycle to maximal strain per second). The voltage was monitored continuously while applying $i = 5$ mA (Keithley 2400 SourceMeter). The stretcher and the measurement equipment were controlled and synchronized using customized software based on LabVIEW 2015 (National Instruments).

Immunohistochemistry. Perfused postmortem tissue was cryoprotected in 30% sucrose in PBS for 48 h before being embedded in cryomatrix (Tissue Tek O.C.T, Sakura Finetek Europe B.V.) and freezing. Then, 30- μ m-thick transverse sections of the spinal cord were cut on a cryostat (Leica), immediately mounted on glass slides and dried. Sections were blocked with 10% bovine serum albumin in PBS for 60 min. Then sections were incubated with the following primary antibodies diluted in blocking solution at room temperature overnight: rabbit anti-glial fibrillary acidic protein (1:1,000, Dako, catalog no. Z0334), anti-Iba1 (1:1,000, FUJIFILM Wako, catalog no. 019-19741). Slides were washed four times with PBS before the secondary antibodies (Alexa Fluor Conjugated, Invitrogen) were applied for 90 min in blocking solution (Alexa). Slides were washed four times with PBS and cover slipped with Mowiol. Immunofluorescence was imaged digitally using a slide scanner (Olympus VS-120 Slide scanner) or confocal microscope (Zeiss, catalog no. LSM880 + Airy fast module with ZEN 2 Black software (Zeiss)). Images were digitally processed using ImageJ NIH software or Imaris (Bitplane, v9.0.0).

FISH. Motor neurons were examined for co-localization of *fos* messenger RNA using the RNA-labeling kit from Molecular Instruments. Sections on slides were covered with 5 \times SSCT (20 \times saline-sodium citrate (SSC) buffer, Invitrogen; 10% Tween 20, Applichem) for 10 min, and then prehybridized in 30% probe hybridization buffer (Molecular Instruments) for 30 min at 37 °C. Sections were hybridized overnight at a 2- μ M probe concentration (for *fos* or *parvalbumin*) in 30% probe hybridization buffer at 37 °C. After hybridization, slides were washed in a solution of 30% probe wash buffer (Molecular Instruments) and 5 \times SSCT four times for 15 min. Sections were then incubated in an amplification buffer (Molecular Instruments) for 30 min at room temperature. In the meantime, fluorophore-labeled HCR hairpins (Molecular Instruments) were snap-cooled (heating at 95 °C for 90 s) and cooled down to room temperature. Amplification was performed overnight at room temperature at a concentration of 120 nM per hairpin in the amplification buffer. After amplification, samples were washed in 5 \times SSCT for at least twice for 30 min to remove unbound hairpins. Last, sections were air dried and cover slipped using Mowiol (Calbiochem).

Clearing by iDisco+. The mouse spinal cord and brains were processed with the iDisco+ for 3D imaging⁴⁶. The detailed protocol and recommended antibody concentrations can be found on the following website: <http://www.idisco.info>.

Three-dimensional imaging of cleared samples. Imaging was performed using a customized MesoSPIM light-sheet microscope⁴⁷. Images were acquired with a $\times 2$ objective when using the MesoSPIM. At $\times 2$ magnification on the MesoSPIM, the pixel resolution was $3.26 \times 3.26 \times 3.00 \mu\text{m}^3$ in x , y and z directions. Image acquisition generated 16-bit TIFF files, and stitching of files was performed using arivis Vision4D (Arivis AG). Imaris (Bitplane, v9.0.0) and arivis Vision4D (Arivis AG) were used to generate 3D reconstructions and optical sections of the raw images.

Statistics and reproducibility. All data are reported as mean \pm s.e.m. unless stated otherwise. Behavioral assays were replicated several times (three to ten times depending on the experiments) and averaged per animal. Statistics were then performed over the mean of the animals. Statistical analysis was performed in GraphPad Prism using two-sided, paired or unpaired Student's t -tests, one-way analysis of variance (ANOVA) for neuromorphological evaluations with more than two groups, and one- or two-way, repeated-measure ANOVA for functional assessments, when data were distributed normally. Post-hoc Tukey's or Bonferroni's test was applied when appropriate. The significance level was set as $P < 0.05$. The nonparametric Mann-Whitney U -test or Wilcoxon's signed-rank test was used when comparisons involved fewer than five mice. Fluorescent labeling of structures targeted by viral vector injections were confirmed in every experimental animal. If labeling was absent, the mice were excluded from the study. If labeling was present, it was similar across the mice.

Reporting Summary. Further information on research design is available in the Nature Research Reporting Summary linked to this article.

Data availability

Source data are provided with this paper.

References

- Capogrosso, M. et al. Configuration of electrical spinal cord stimulation through real-time processing of gait kinematics. *Nat. Protoc.* **13**, 2031–2061 (2018).
- Mathis, A. et al. DeepLabCut: markerless pose estimation of: user-defined body parts with deep learning. *Nat. Neurosci.* **21**, 1281–1289 (2018).
- Watson, C., Paxinos, G., Kayalioglu, G. & Heise, C. Atlas of the mouse spinal cord, in *The Spinal Cord* (Academic Press, 2009).
- Yaroslavsky, A. N. et al. Optical properties of selected native and coagulated human brain tissues in vitro in the visible and near infrared spectral range. *Phys. Med. Biol.* **47**, 2059 (2002).
- Mignon, C., Tobin, D. J., Zeitouny, M. & Uzunbajakava, N. E. Shedding light on the variability of optical skin properties: finding a path towards more accurate prediction of light propagation in human cutaneous compartments. *Biomed. Opt. Express.* **9**, 852–872 (2018).
- Bashkatov, A. N. et al. In-vitro study of control of human dura mater optical properties by acting of osmotic liquids. In *Controlling Tissue Optical Properties: Applications in Clinical Study* (SPIE, 2000).
- Renier, N. et al. IDISCO: a simple, rapid method to immunolabel large tissue samples for volume imaging. *Cell* **159**, 896–910 (2014).
- Voigt, F. F. et al. The mesoSPIM initiative: open-source light-sheet microscopes for imaging cleared tissue. *Nat. Methods* **16**, 1105–1108 (2019).

Acknowledgements

We thank B. Schneider for providing viral vectors, and L. Batti and S. Pagès from the ALiCe platform for light-sheet imaging. Financial support was provided by a Consolidator Grant from the European Research Council (ERC-2015-CoG HOW2WALKAGAIN 682999), the Swiss National Science Foundation (subsidies 310030_130850, CRSII5_183519, BSCG10 1578000) and the European Union's Horizon 2020 Framework Programme for Research and Innovation under the Specific Grant agreement no. 785907 (Human Brain Project SGA2) and the Bertarelli Foundation. C.K. is supported by a Marie Skłodowska-Curie postdoctoral fellowship and HFSP long-term fellowship (LT001278/2017-L). S.S. and C.I.D.Z. are supported by grants from BIG (Erasmus MC), Medical-NeuroDelta and INTENSE (LSH-NWO).

Author contributions

C.K., F.M., P.S., G.C. and S.P.L. contributed equally to this work. F.M. developed and collaborated with V.P. and K.K. for the production of spinal implants. C.K., F.M., I.F., S.S. and T.H.H. carried out the experiments and analysis. P.S., N.B. and Q.H. developed the head-mounted wireless stimulation device. I.J. performed MRI. A.P. carried out the high-speed X-ray videography. A.R. and J.G. analyzed the imaging data. A.R. and N.A. conducted computational simulations. J.R. generated the figures and conceived the illustrations with contributions from C.K., F.M. and P.S. S.P.L. and G.C. conceived and supervised the study. G.C. and S.P.L. secured funding. G.C. wrote the paper with S.P.L., C.K., F.M. and P.S., and all the authors contributed to its editing.

Competing interests

The authors declare competing interests: G.C. and S.P.L. are founders and shareholders of Onward medical, a company with partial relationship to the present work.

Additional information

Extended data Extended data are available for this paper at <https://doi.org/10.1038/s41587-021-01019-x>.

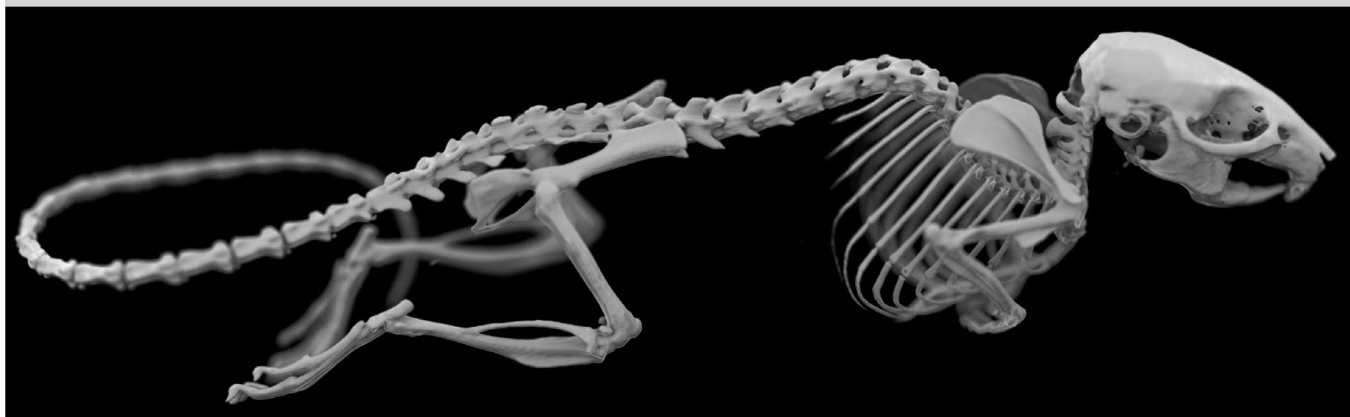
Supplementary information The online version contains supplementary material available at <https://doi.org/10.1038/s41587-021-01019-x>.

Correspondence and requests for materials should be addressed to Stéphane P. Lacour or Grégoire Courtine.

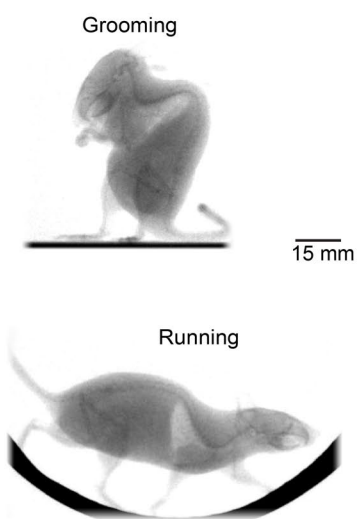
Peer review information *Nature Biotechnology* thanks C. J. Heckman and the other, anonymous, reviewer(s) for their contribution to the peer review of this work.

Reprints and permissions information is available at www.nature.com/reprints.

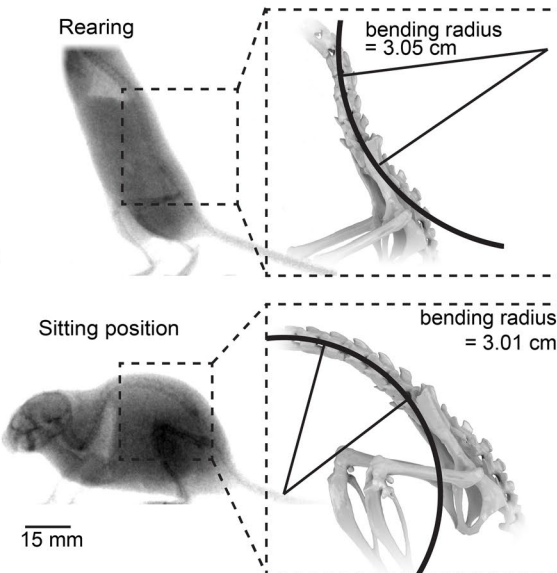
Step 1: Computerized Tomography of the entire mouse to reconstruct the skeleton in 3D



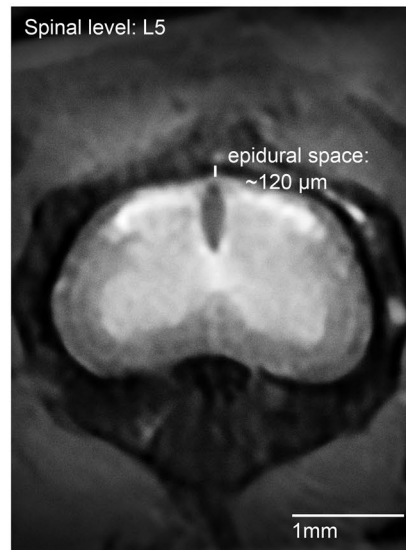
Step 2: High-speed X-ray videography



Step 3: Bending radius quantification

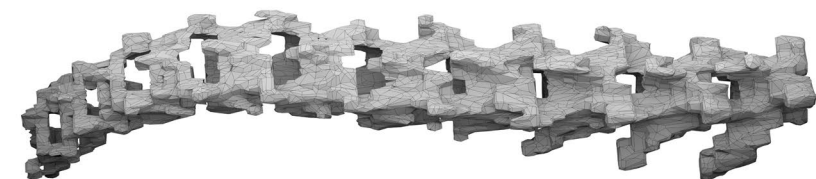


Step 4: High-resolution MRI



Step 5: Finite element models of the mouse lumbar spine to provide estimates of suitable dimensions for spinal implants

Reconstructed bones from MRI and CT



Reconstructed spinal cord and rootlet modeling



Combined model

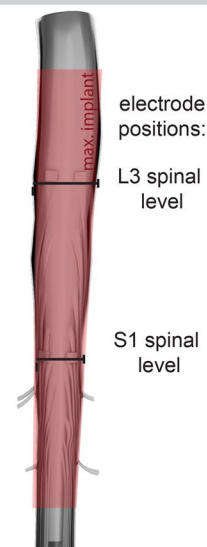


Maximum dimensions allowed:

Width: ~4mm (roots exiting from vertebrae)

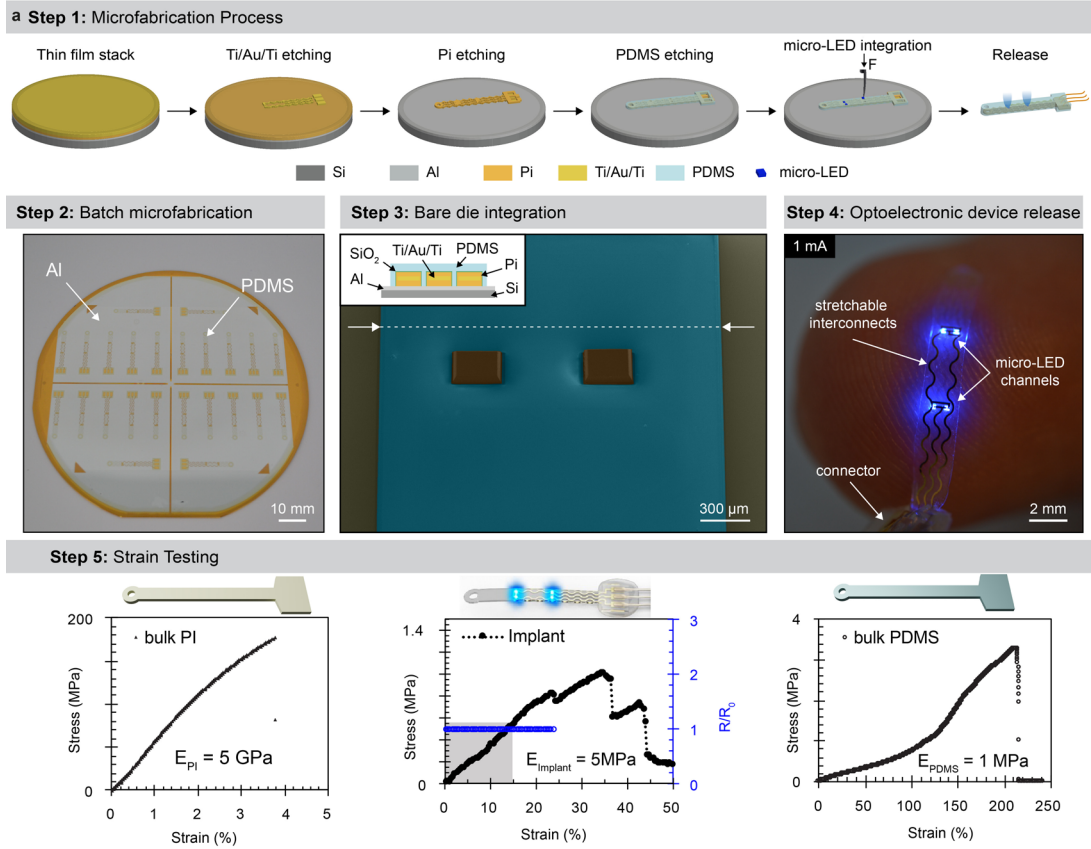
Thickness: ~120μm (epidural space)

Length: ~1cm (lumbar enlargement)

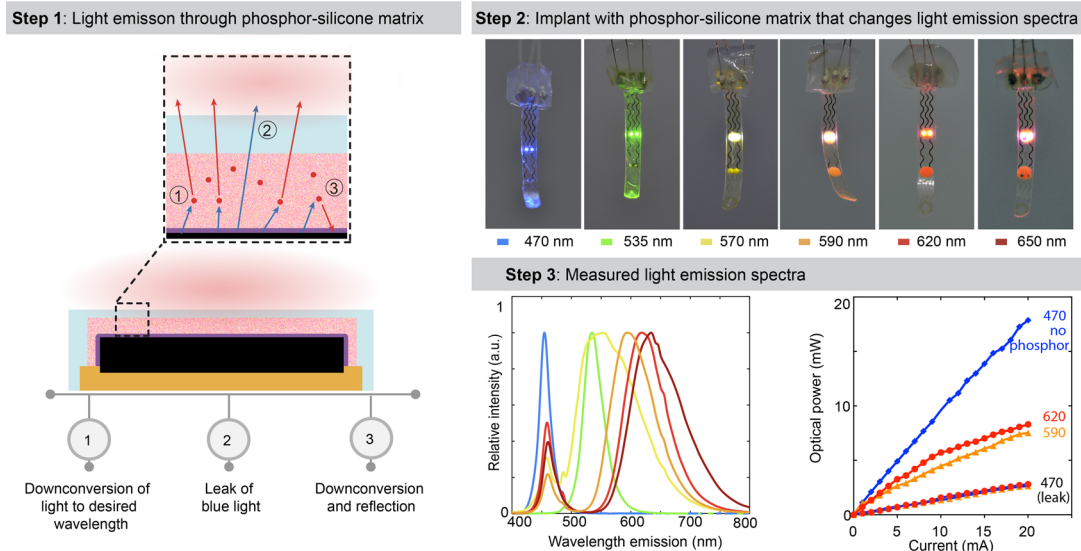


Extended Data Fig. 1 | See next page for caption.

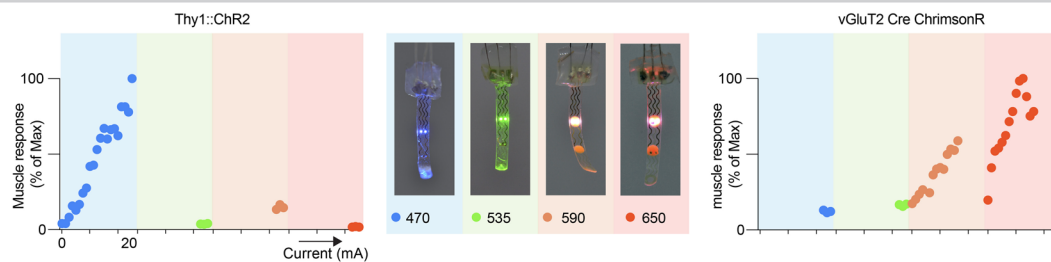
Extended Data Fig. 1 | Three-dimensional anatomical model of the mouse. **Step 1:** The entire mouse was imaged in a computed tomography (CT) scanner. The resulting reconstruction of the entire skeleton of the mouse is shown. **Step 2:** We acquired high-speed X-ray videographies of a freely behaving mouse, which allowed to capture the extent of the changes in postures of the mouse during activities of daily living. **Step 3:** The reconstructed mouse skeleton is morphed onto selected X-ray images to quantify the bending radius of the lumbar spinal cord. **Step 4:** We adapted an antenna to enable magnetic resonance imaging of the lumbar spinal cord, including the visualisation of the posterior roots. We measured the epidural space in these images. **Step 5:** We transformed these imaging datasets into finite element models of the mouse lumbar spinal cord, including the vertebra, spinal cord and spinal roots. This computer model provides estimates of the suitable dimensions for an implant in the epidural space of the lumbar spinal cord of mice shown in red.



b Wavelength downconversion with phosphor-silicone matrix



Step 4: Testing specificity of the photostimulation using implants with different coloured emission spectra



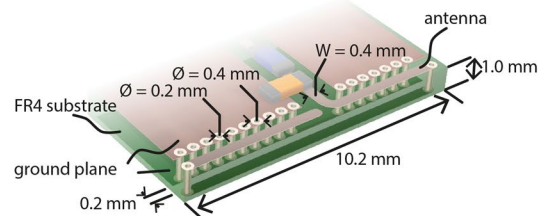
Extended Data Fig. 2 | See next page for caption.

Extended Data Fig. 2 | Fabrication process of the micro-LED array. a, Main steps of the microfabrication of the micro-LED array: **Step 1:** Schematic illustration of the micro-LED array microfabrication process. A Ti/Au/Ti film is sputtered on a polyimide substrate and subsequently patterned by photolithography and wet etching. Next, the device interconnects are covered by a 2nd layer of polyimide, and the whole polyimide stack is patterned by photolithography and reactive ion etching (RIE). The preparation is covered with a thin layer of PDMS. The silicone superstrate is patterned to the device layout by photolithography and RIE, exposing the micro-LED integration sites. Then, micro-LEDs are precisely interfaced with the device interconnects. Finally, the micro-LED array is encapsulated with PDMS and released from the silicon carrier. **Step 2:** Photograph of the 4-inch wafer following the micro-LED array microfabrication process. **Step 3:** Colorized scanning electron micrograph (45° tilted view) of the micro-LED array surface, highlighting the fine patterning of the PDMS superstrate and integration of the bare dies. Schematic cross-section of the device, showing three interconnects encapsulated in PDMS, top left inset. **Step 4:** Photograph of the optoelectronic device laminated on a fingertip. The array hosts 2 independent micro-LED channels, connected via serpentine interconnects that accommodate physiological motion. **Step 5:** Stress-strain curves for bulk PI, a fully functional implant and bulk PDMS measured under a displacement rate of 100 μm/s. In the panel referring to the fully functional implant, the y-axis on the right (blue) also reports the relative resistance measured at the current input of 1 mA. The grey box highlights the strain range under in vivo conditions. **b,** Downconversion of light to desired wavelength. **Step 1:** Schematic illustration of the downconversion process using a phosphor-silicone matrix. Blue photons are converted to the desired wavelength (1), transmitted through the matrix (2) or back-scattered (3). **Step 2:** Photographs of the optoelectronic devices with the introduction of the phosphor-silicone matrix. The phosphor peak emission wavelengths are indicated below the corresponding photographs. **Step 3:** Optical characterization following downconversion of blue light. Emission spectra of the micro-LED arrays depending on their respective phosphor-silicone matrix implementation. Note the leakage of blue light at $\lambda = 470$ nm (left). Total optical power produced by one micro-LED channel covered with phosphor-silicone matrices with emission peaks at $\lambda = 590$ nm or $\lambda = 620$ nm. The respective optical power of the leaked blue light is depicted at $\lambda = 470$ nm. For reference, the optical power of bare blue LEDs is plotted. **Step 4:** Characterisation of different wavelength implants in Thy1-ChR2 and vGlut 2 ChrimsonR mice. Only 470 nm wavelength light results in muscle responses in Thy1-ChR2 mice. Only 590 nm and 650 nm wavelengths result in muscle responses in vGlut 2 ChrimsonR mice.

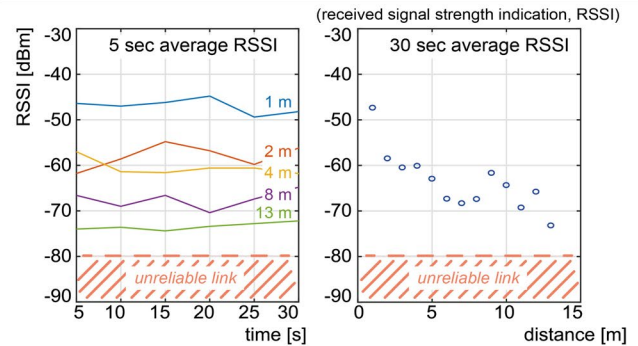
Step 1: System overview



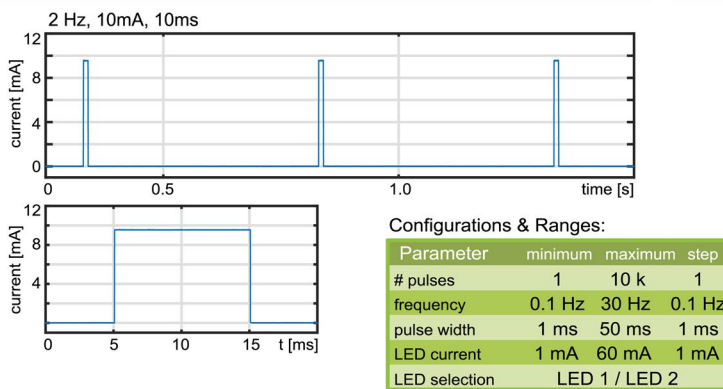
Step 2: 3D-microstrip antenna design



Step 3: Wireless link characterisation



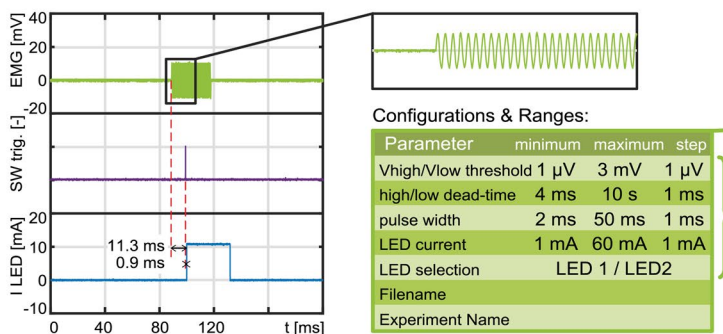
Step 4: LED current pulse train measurements



Step 5: Android user interface for photostimulation experiments



Step 6: Closed-loop delay characterisation



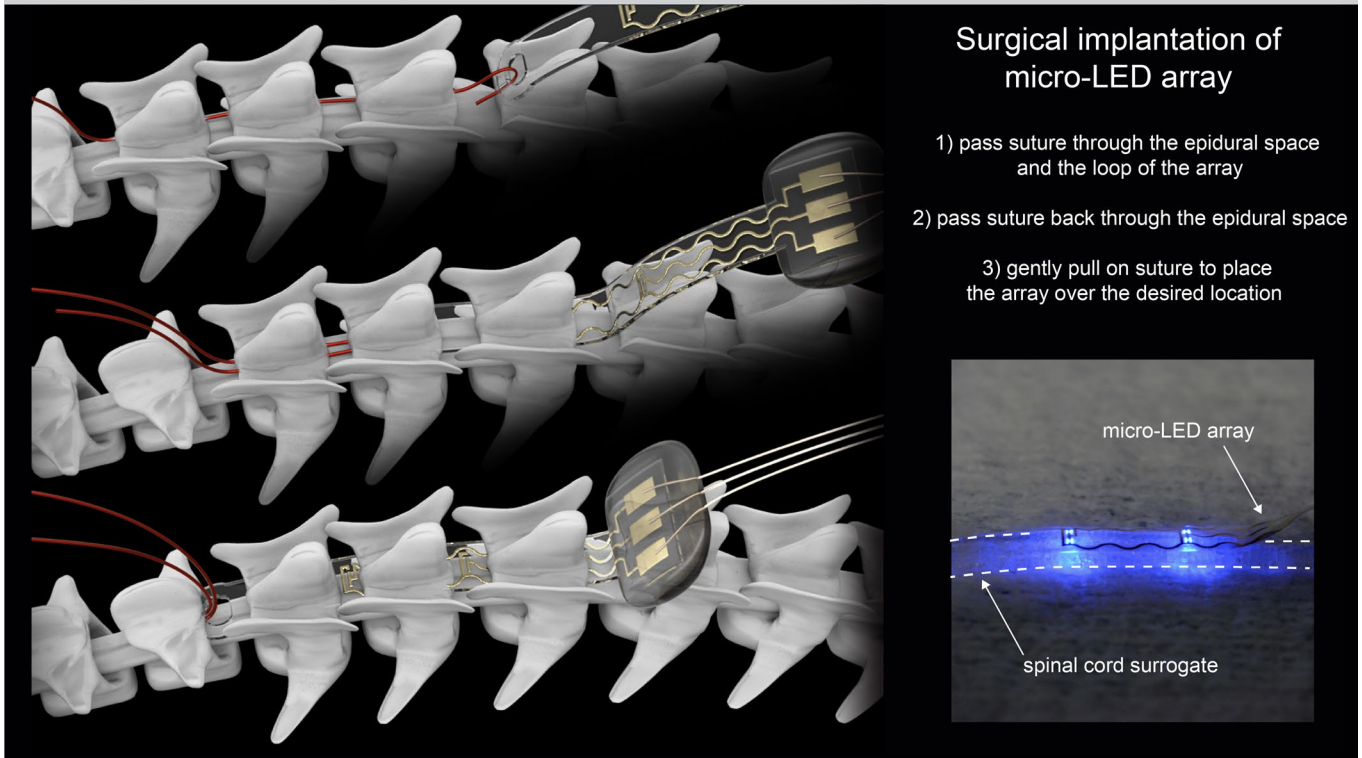
Step 7: Android user interface for closed-loop experiments



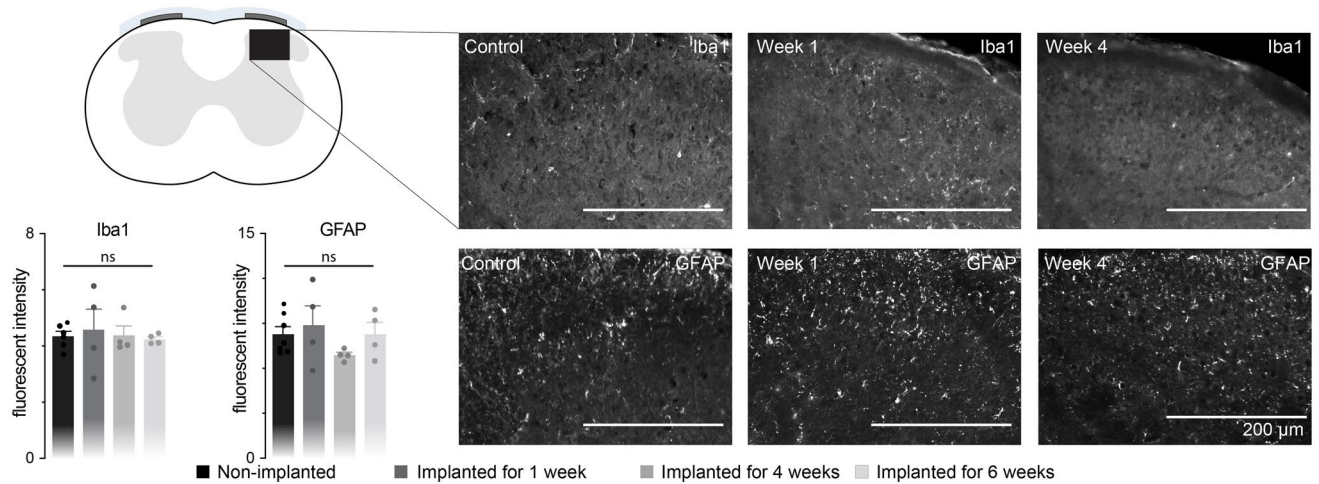
Extended Data Fig. 3 | See next page for caption.

Extended Data Fig. 3 | Ultraminiaturized, battery powered, head-mounted, wireless recording and stimulation platform. Step 1: System overview: the implants (9 stainless steel wires for ground and 4 differential EMG recording channels, micro-LEDs connected by 3 copper wires) are connected by a 16 pin Omnetics connector to the PCB assembly of the wireless headstage platform. **Step 2:** Illustration of the antenna design as integrated on the PCB of the head-stage. **Step 3:** Head-stage wireless link reliability assessment in a typical laboratory/office environment based on received signal strength indication (RSSI) measurements versus line-of-sight distance. A sufficient link is maintained for over 10 m of distance. **Step 4:** Verification of the LED pulsed current driver performance: LED current can be controlled in 1 mA steps and is monitored on-chip for each issued pulse to verify micro-LED-implant condition and ensure experiment validity. **Step 5:** Tablet user interface for pulse(-train) stimulation and configuration ranges for all parameters. **Step 6:** Measurement of closed-loop performance: a EMG signal, simulated as a short sine-wave burst, the triggering of the software algorithm (SW trig), and the issued LED current pulse (1 LED) have been acquired by an oscilloscope to measure the delay between the beginning of EMG activity and the closed-loop response. A delay of 11.3 ms is caused by the signal processing, which includes characteristics preventing spiking caused by noise (low-pass). A delay of 0.9 ms is caused by the construction of signal to drive the LED activation. **Step 7:** Tablet user interface for closed-loop experiments, consisting of an experiment parameter configuration interface and a live preview of all four acquired EMG traces.

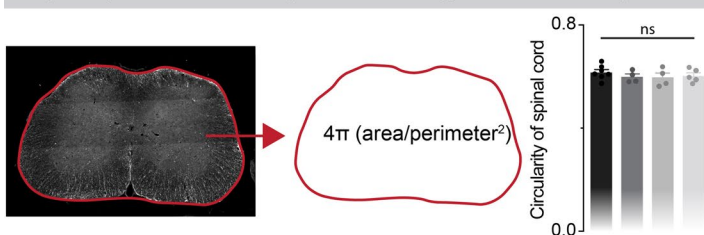
Step 1: Surgical insertion of the spinal implant



Step 2: Histological confirmation of biointegration



Step 3: Spinal cord circularity does not change after chronic implantation



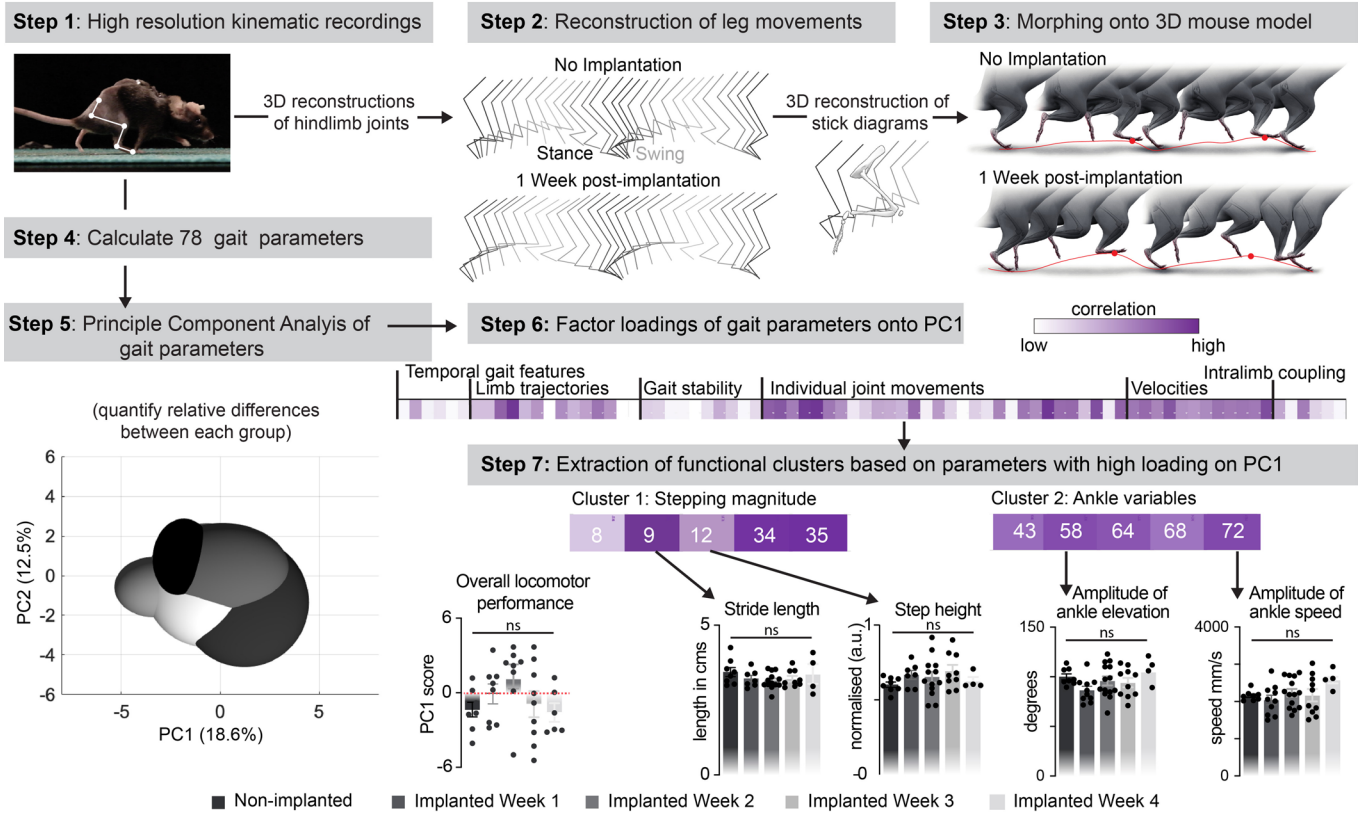
Step 4: Copper wires do not cause excessive tissue response



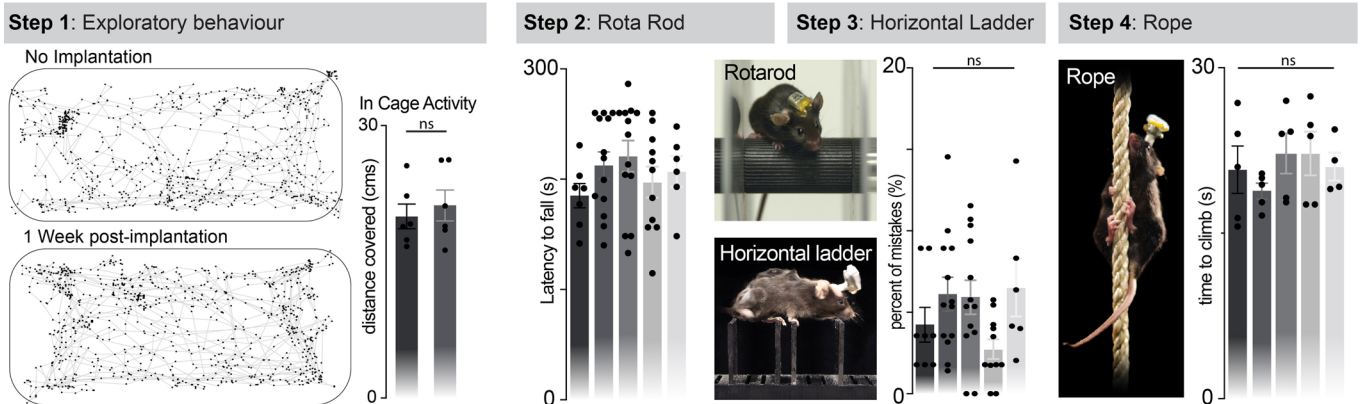
Extended Data Fig. 4 | See next page for caption.

Extended Data Fig. 4 | Long-term biointegration of the micro-LED array. Step 1: Stepwise surgical insertion of the micro-LED array into the epidural space. Micro-LED array overlaying a spinal cord surrogate, bottom right inset. **Step 2:** Post-mortem evaluation of foreign body responses within the dorsal horn of spinal segments located below the micro-LED array. Coronal spinal cord sections of mice implanted for 1, 4 or 6 weeks were stained against Iba1 and GFAP proteins, and compared with the spinal cord of non-implanted mice. Histogram plots report the fluorescent staining intensity quantified within the dorsal horns. The photograph shows the staining from a window within the dorsal horn, as shown in the scheme ($n = 6$ healthy mice, $n=4$ for each timepoint post-implantation one-way ANOVA, Iba1 $p = 0.64$, GFAP $p = 0.36$, $\text{mean} \pm \text{s.e.m.}$). **Step 3:** Schematic illustrating the post-mortem evaluation of spinal cord circularity. The bar graph reports the mean circularity ($n=6$ mice, one-way ANOVA, $p = 0.95$, $\text{mean} \pm \text{s.e.m.}$). **Step 4:** Photographs show examples of subcutaneous wires taken in mice that were implanted for 4 weeks.

a Kinematic analysis of locomotion



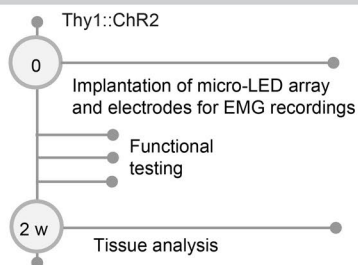
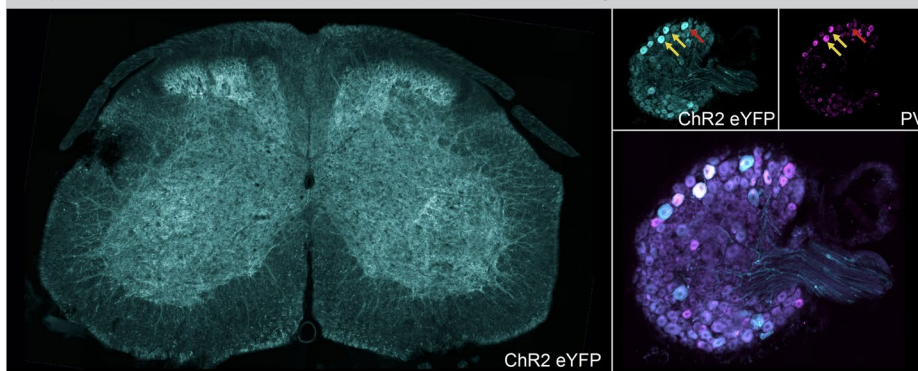
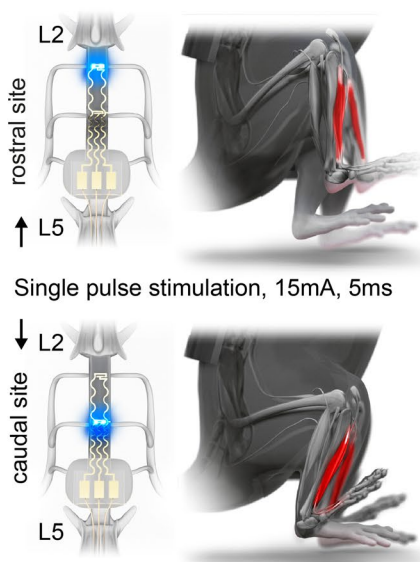
b Exploratory behaviour and fine motor function



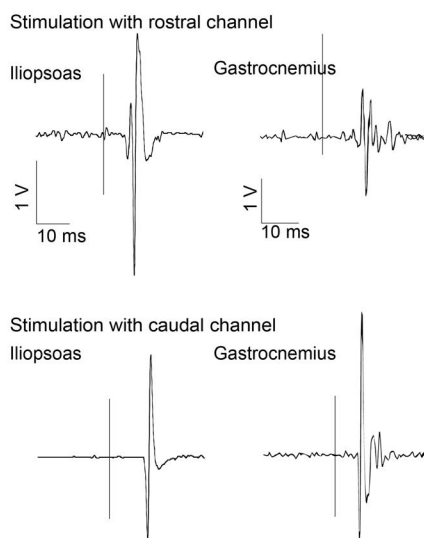
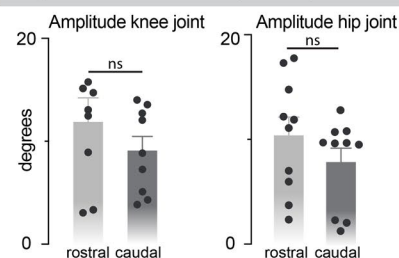
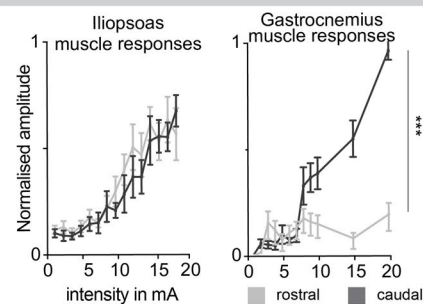
Extended Data Fig. 5 | See next page for caption.

Extended Data Fig. 5 | The micro-LED array does not alter motor functions and behaviors. a, Kinematic analysis of locomotor function reveals there are no gait deficits after micro-LED implantation. **Step 1:** The absence of influences on locomotor performance was evaluated using longitudinal recordings of whole-body kinematics during walking along a corridor. Markers are attached to the skin overlaying anatomical landmarks to record whole-body kinematics with the optoelectronic Vicon system. **Step 2:** Sequence of leg movements during walking reconstructed from the 3D coordinates of the markers. **Step 3:** The kinematics is morphed onto the anatomical model of the mouse and an envelope is added over the bony structure to obtain a realistic reconstruction of leg movements during walking. The resulting chronophotography-like sequences of locomotor movements illustrate the absence of differences between gait patterns recorded before and after the implantation. **Step 4:** A total of 78 parameters were calculated from kinematic recordings (Supplementary Table 1). **Step 5:** A principal component (PC) analysis was applied to the calculated parameters, and represented in the new space created by PC1 and PC2. Each dot represents the mean and SEM values of many mice ($n > 5$ mice) with averaged data from many gait cycles ($n > 10$ pre mouse). The bar plot reports the mean values of scores on PC1, which captures the more pronounced differences between gait cycles recorded at different time-points ($n=6-9$ mice/timepoint, one-way ANOVA, $p = 0.16$, $\text{mean} \pm \text{s.e.m.}$). **Step 6:** Color-coded representation of factor loadings with the highest level of correlation of PC1. **Step 7:** Functional clusters of highly correlated parameters were extracted from PC1 loadings representing gait parameters that describe differences between groups the most. Bar plots reporting mean values of calculated gait parameters with high correlations with PC1. This highly-sensitive statistical analysis failed to detect measurable changes in gait patterns following the implantation of the micro-LED array ($n=6-9$ mice, one-way ANOVAs, Stride length $p = 0.42$; Step height $p=0.46$; Amplitude of ankle elevation $p=0.13$; Amplitude of Ankle Speed $p=0.13$, $\text{mean} \pm \text{s.e.m.}$).

b, Implantation of the micro-LED had no effect on exploratory behaviours or fine locomotor function. **Step 1:** The potential impact of the micro-LED array on exploratory behaviours was measured in the open field paradigm. Body trajectories measured during 20 min of home cage monitoring are shown before and after implantation of micro-LED array. The bar plot reports the quantification of distance covered during 20 min period of observation ($n = 6$, two-sided unpaired t-test, $p = 0.58$, $\text{mean} \pm \text{s.e.m.}$). **Step 2:** Mice were tested on the accelerating rotarod paradigm. The bar plot reports quantification of the time to fall off ($n = 12$ mice per timepoint, $n=6$ mice at week 4, one-way ANOVA, $p = 0.44$, $\text{mean} \pm \text{s.e.m.}$). **Step 3:** Mice walked along a horizontal ladder with unevenly spaced rungs. The bar plot reports quantification of the percentage of foot falls ($n = 8$ mice, one-way ANOVA, $p = 0.08$, $\text{mean} \pm \text{s.e.m.}$). **Step 4:** Mice climbed up a 1-meter long vertical rope. The bar plot reports quantification of the time to complete the climb ($n = 5$ mice, one-way ANOVA, $p = 0.60$, $\text{mean} \pm \text{s.e.m.}$).

Step 1: Timeline of experiment**Step 2: Post-mortem characterization of ChR2 expression in Thy1::ChR2 eYFP mice****Step 3: Functional testing**

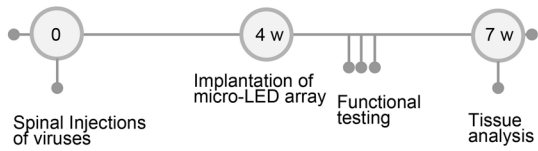
Single pulse stimulation, 15mA, 5ms

Step 4: Muscle activity recordings**Step 5: Quantification of joint angle****Step 6: Quantification of muscle responses**

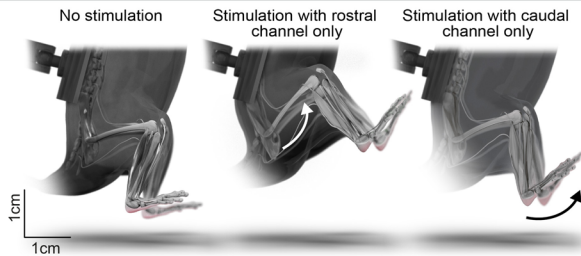
Extended Data Fig. 6 | Spatially targeted photostimulation elicits robust muscle responses. **Step 1:** Timeline detailing key experiments. **Step 2:** Post-mortem verification of ChR2 expression. Photographs show the robust expression of ChR2 in the spinal cord and dorsal root ganglia of Thy1-ChR2 mice. ChR2 is expressed in proprioceptive neurons of the dorsal root ganglia, as illustrated with the overlap between ChR2-eYFP with *parvalbumin* mRNA (HCR). **Step 3:** Experimental set up to evaluate muscle responses and leg kinematics when delivering single pulses of photostimulation while the mouse is suspended in the air in a robotic body weight support system. Leg movements are reconstructed following one pulse of photostimulation delivered over the rostral versus caudal lumbar spinal cord. **Step 4:** Associated muscle responses in the iliopsoas and gastrocnemius medialis muscles are shown following one pulse of photostimulation delivered over the rostral versus caudal lumbar spinal cord. **Step 5:** The bar plot reports the mean range of motion at the knee and hip following photostimulation over the rostral and caudal lumbar spinal cord ($n = 10$ mice, two-sided unpaired t-test, $p = 0.2445$ and $p = 0.3153$ respectively, mean \pm s.e.m.). Note that the iliopsoas muscle is activated by photostimulation of rostral lumbar segments, as expected based on the anatomical position of the motoneurons innervating this muscle within these spinal segments and pre-motor interneurons, as well as by photostimulation of caudal lumbar segments through the activation of primary afferent fibres embedded in the rostral posterior roots that travel along the spinal cord, in the vicinity of the caudal LED channel. The different location at which photostimulation depolarizes afferent fibers is reflected in the increase in the latency of muscle responses with photostimulation over caudal versus rostral lumbar segments and the clear singular wave. **Step 6:** The plots report the area under the curve (AUC) of rectified muscle responses of the iliopsoas and gastrocnemius following photostimulation of the rostral versus caudal lumbar spinal cord with increasing intensity ($n = 5$ mice, one-way ANOVA, ***, $p < 0.0001$, mean \pm s.e.m.).

a Targeted photostimulation of the lumbar spinal cord in vGluT2 Cre mice

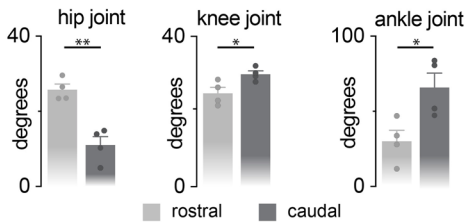
Step 1: Timeline of experiment



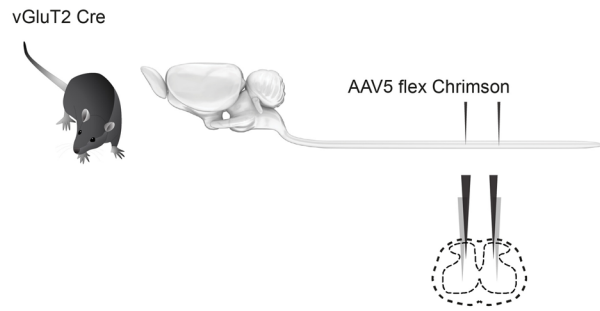
Step 3: Functional testing



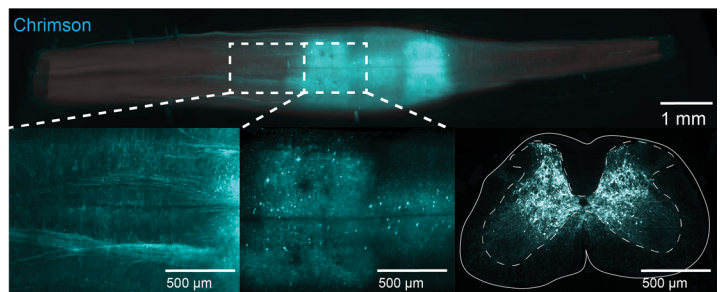
Step 4: Quantification of leg kinematics



Step 2: Intersectional genetics to target vGluT2^{ON} Interneurons

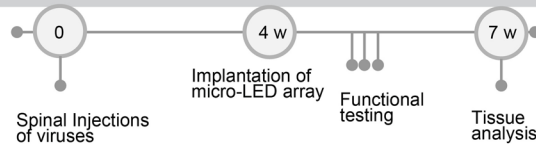


Step 5: Post-mortem verification of Chrimson expression

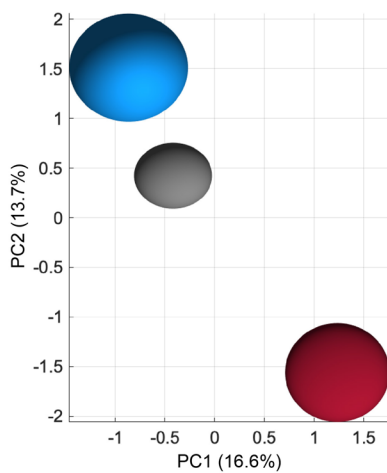


b Two-colour optogenetic activation and silencing of vGluT^{ON} neurons in the same mouse

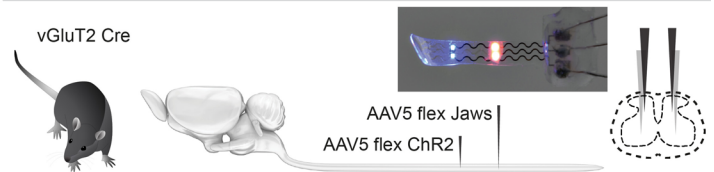
Step 1: Timeline of experiment



Step 3: Kinematic analysis of gait patterns



Step 2: Intersectional genetics to target vGluT^{ON} Interneurons



Step 4: Factor loadings of gait parameters onto PC1

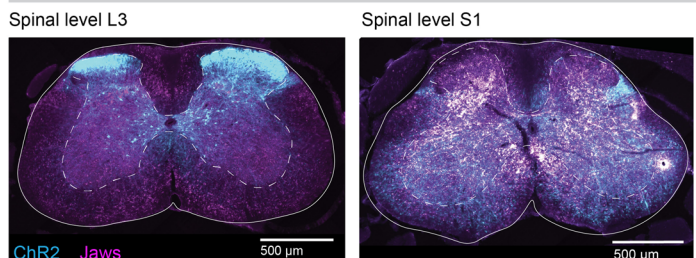


Step 5: Functional clusters to identify the most affected variables

Cluster 1: Parameters relating to Step height

12 13 32 33 34 35 41 52 56

Step 6: Post-mortem verification of Jaws and ChR2 expression

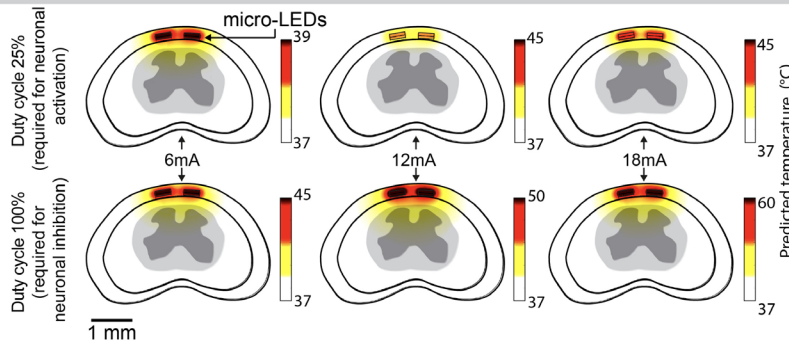


Extended Data Fig 7 | See next page for caption.

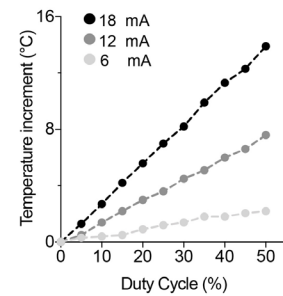
Extended Data Fig 7 | Conversion of emitted light to target any opsin. a, Targeted photostimulation of vGlut2^{ON} neurons in the spinal cord results in distinct hip versus ankle movements. **Step 1:** Timeline detailing key experiments. **Step 2:** Schematic illustration of the experimental procedures to target vGlut2^{ON} spinal neurons with Chrimson expression. **Step 3:** Leg movements are reconstructed following one pulse of photostimulation delivered over the rostral versus caudal lumbar spinal cord. 620 nm photostimulation in vGlut2 mice, injected with an AAV flex ChrimsonR around motor pools of the iliopsoas and tibialis anterior, results in more specific muscle activation patterns. Rostral photostimulation maximises the hip flexor amplitude and caudal photostimulation maximises the foot flexor amplitude. **Step 4:** The bar plot reports the mean range of motion at the hip, knee and ankle following photostimulation over the rostral and caudal lumbar spinal cord (n = 10 mice, two-sided unpaired t-test, p = 0.0015; 0.0265; 0.0180 respectively, mean ± s.e.m.). **Step 5:** Post-moterm verification of Chrimson expression. Photographs show the robust expression of Chrimson in the spinal cord in vGlut2 Cre mice around the injection sites, which was assessed with iDISCO. **b,** Two-colour optogenetic activation and inhibition of vGlutON neurons in the spinal cord. **Step 1:** Timeline detailing key experiments. **Step 2:** Schematic illustration of the experimental procedures to target vGlut2^{ON} spinal neurons with ChR2 and Jaws expression and the micro-LED array implanted over the injection sites. **Step 3:** A series of 78 gait parameters (see Supplementary Table 1) calculated from the kinematic recordings are submitted to a PC analysis. Each recorded gait pattern, depicted by each dot, are shown in the new denoised space defined by PC1 and PC2. **Step 4:** Factors loadings of individual parameters on PC1 (correlation between PC1 and each variable). **ar.** **Step 5:** Functional clusters of highly correlated parameters were extracted from PC1 loadings representing gait parameters that describe differences between groups the most. Parameters relating to step height explained a large variance of the gait cycles, therefore indicating it best describes differences between groups. **Step 6:** Post-moterm verification of ChR2 and Jaws expression. Photographs show the robust expression of ChR2 and Jaws in the spinal cord in vGlut2 Cre mice at spinal level L3 (targeted with ChR2) and spinal level S1 (targeted with Jaws). Note: Fibers of vGlut^{ON} neurons project across many levels of the spinal cord and were therefore detected at both levels.

a Simulating heat diffusion in spinal cord tissue

Step 1: Maximum temperature calculated with Bioheat Transfer model

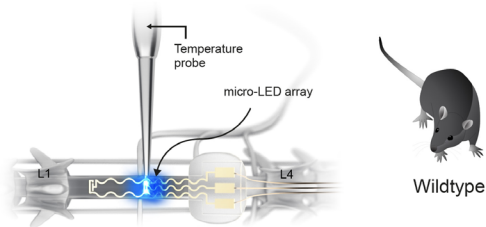


Step 2: Temperature increase in air

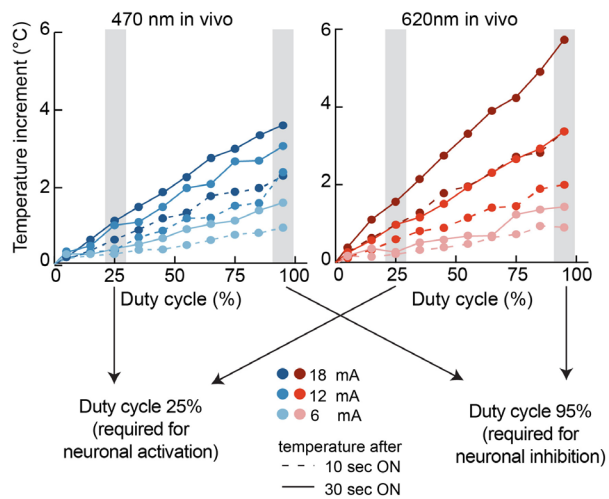


b Measuring heat diffusion in tissues: intraspinal heat probe measurements

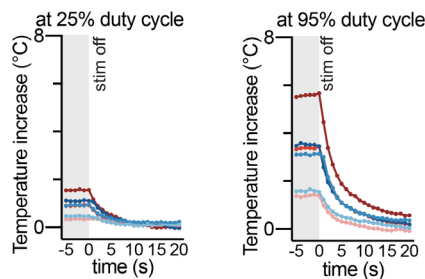
Step 1: Experimental set-up



Step 2: In vivo measurements of temperature increments

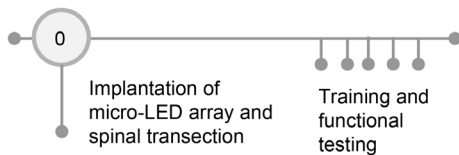


Step 3: Temperature decay after photostimulation

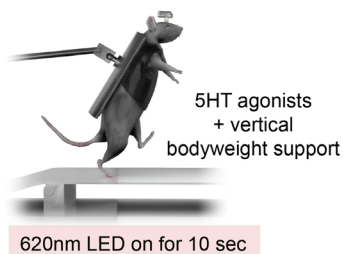


c Photostimulation generates heat that affects motor function

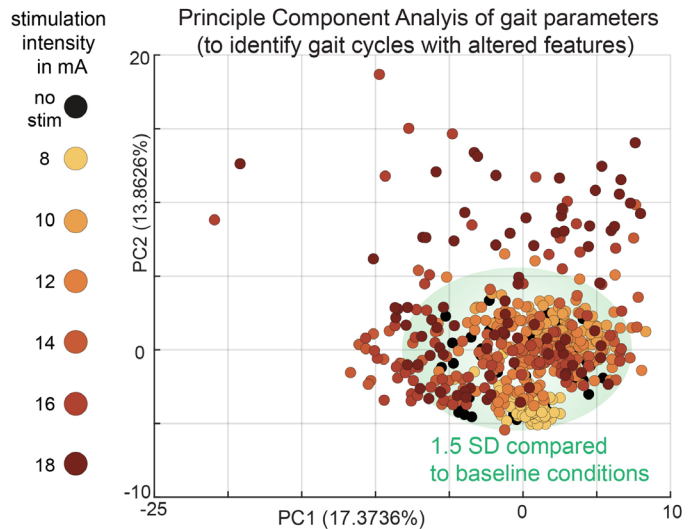
Step 1: Timeline of experiment



Step 2: Functional testing



Step 3: Kinematic analysis

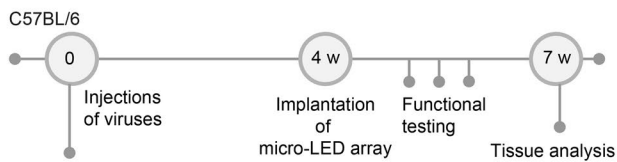


Extended Data Fig 8 | See next page for caption.

Extended Data Fig 8 | Heat diffusion in the mouse spinal cord and its consequence for motor control. **a**, Simulating heat diffusion in the spinal cord tissue. **Step 1:** Maximum temperature calculated with the Bioheat Transfer model in response to photostimulation protocols eliciting activation of ChR2 (25% duty cycle) or Jaws (95% duty cycle). Each plot has an adjusted scale allowing to view the maximum temperatures. **Step 2:** Temperature measurements of the LEDs in air with an infrared camera confirming maximum temperatures predicted by the model. **b**, Heat diffusion measure in vivo with a temperature probe. **Step 1:** Experimental setup. **Step 2:** Relationship between incremental duty cycles (every 5%) and the increase in temperature measured after 10 s and 30 s for two wavelengths delivered over incremental photostimulation intensity (every 50 mW/mm²). **Step 3:** In vivo measurements of heat decay using a temperature probe inserted in the dorsal horn after 30 s of photostimulation with the settings necessary to target ChR2 (25% duty cycle, wavelength 470 nm, 2 LEDs, left) or Jaws (95% duty cycle, wavelength 620 nm, 2 LEDs, right). The plots report the changes in temperature over time for three levels of intensity. **c**, Heat affecting locomotion in wildtype mice. **Step 1:** Timeline detailing key experiments. **Step 2:** Experimental setup to record leg kinematics during stepping on a treadmill while photostimulation of increasing intensity is delivered over the spinal cord of a mice with a complete SCI. A serotonergic pharmacotherapy is administered prior to the experiment to reactivate the lumbar spinal cord below the injury. **Step 3:** A series of 78 gait parameters (see Supplementary Table 1) calculated from the kinematic recordings are submitted to a PC analysis. Each recorded gait pattern, depicted by each dot, are shown in the new denoised space defined by PC1 and PC2.

a Silencing lumbar projecting reticulospinal neurons

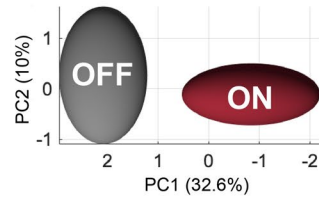
Step 1: Timeline of experiment



Step 3: Functional testing



Step 4: Kinematic analysis



Step 5: Factor loadings of gait parameter onto PC1



Step 6: Functional clusters to identify the most affected variables

Cluster 1: Paw dragging

19 20 4 70 56

Cluster 2: Step height

12 9 31 32 33 34 35

b Silencing lumbar projecting corticospinal neurons

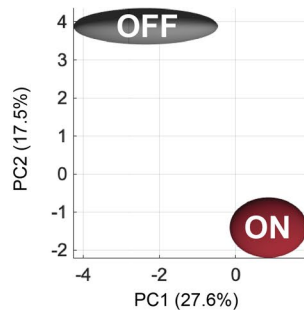
Step 1: Timeline of experiment



Step 3: Functional testing



Step 4: Kinematic analysis



Step 5: Gait parameter loadings onto PC1



Step 6: Functional clusters to identify the most affected variables

Cluster 1: Paw dragging

19 20 55 41 42 57

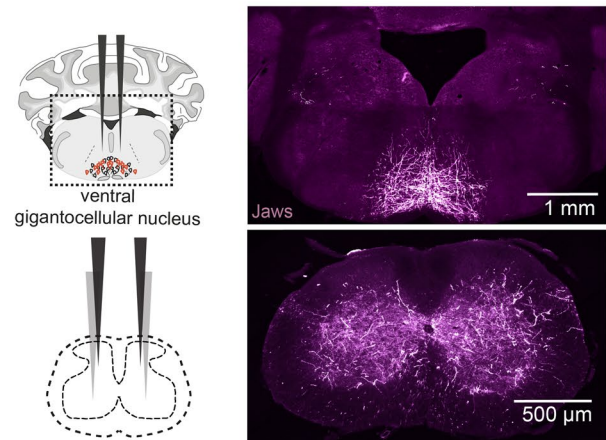
Cluster 2: Balance

23 24 32 33 53

Step 2: Intersectional genetics to target the reticulospinal tract



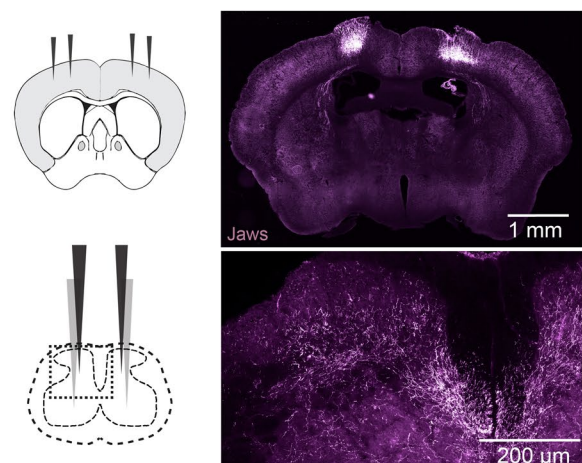
Step 7: Post-mortem verification of Jaws expression



Step 2: Intersectional genetics to target the corticospinal tract



Step 7: Post-mortem verification of Jaws expression

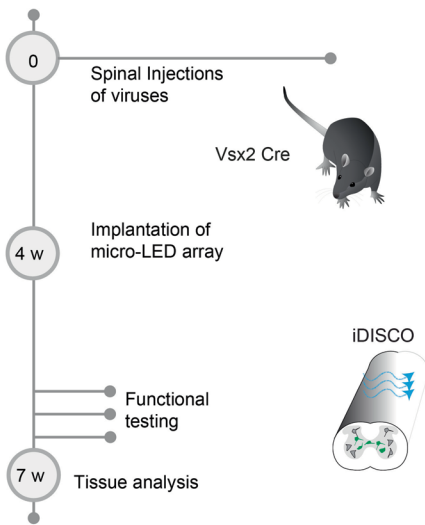


Extended Data Fig 9 | See next page for caption.

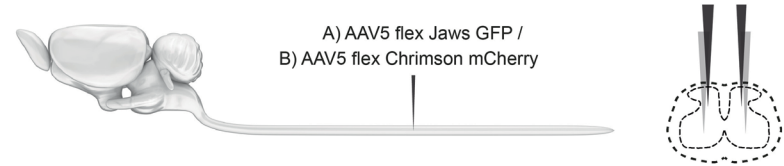
Extended Data Fig 9 | Intersectional genetics to target specific pathways and probe their function. a, Optogenetic silencing of the corticospinal tract in the lumbar spinal cord. **Step 1:** Timeline detailing key experiments. **Step 2:** Schematic illustration of the experimental procedures to target corticospinal tract neurons with synaptic projections to the lumbar spinal cord with Jaws. **Step 3:** Mice are walking freely when the photostimulation is suddenly turned on. **Step 4:** A series of 78 gait parameters (see Supplementary Table 1) calculated from the kinematic recordings are submitted to a PC analysis. Each dot represents the mean and SEM values of many gait cycles ($n > 10$ per mouse) are shown in the new denoised space defined by PC1 and PC2. **Step 5:** Factors loadings of individual parameters on PC1 (correlation between PC1 and each variable). **Step 6:** Functional clusters of highly correlated parameters were extracted from PC1 loadings representing gait parameters that describe differences between groups the most. Parameters relating to paw dragging and balance explained a large variance of the gait cycles, therefore indicating it best describes differences between groups. **Step 7:** Post-mortem verification of Jaws expression. Photographs show the robust expression of Jaws in the lumbar spinal cord, as well as in neurons located in the injected region of the primary motor cortex. **b,** Optogenetic silencing of the reticulospinal tract in the lumbar spinal cord. **Step 1:** Timeline detailing key experiments. **Step 2:** Schematic illustration of the experimental procedures to target reticulospinal tract neurons with synaptic projections to the lumbar spinal cord with Jaws. **Step 3:** Mice are walking freely when the photostimulation is suddenly turned on. **Step 4:** A series of 78 gait parameters (see Supplementary Table 1) calculated from the kinematic recordings are submitted to a PC analysis. Each dot represents the mean and SEM values of many gait cycles ($n > 10$ pre mouse) are shown in the new denoised space defined by PC1 and PC2. **Step 5:** Factors loadings of individual parameters on PC1 (correlation between PC1 and each variable). **Step 6:** Functional clusters of highly correlated parameters were extracted from PC1 loadings representing gait parameters that describe differences between groups the most. Parameters relating to paw dragging and step height explained a large variance of the gait cycles, therefore indicating it best describes differences between groups. **Step 7:** Post-mortem verification of Jaws expression. Photographs show the robust expression of Jaws in the lumbar spinal cord, as well as in neurons located in the ventral gigantocellular nucleus.

a Manipulating V2a interneurons during swimming

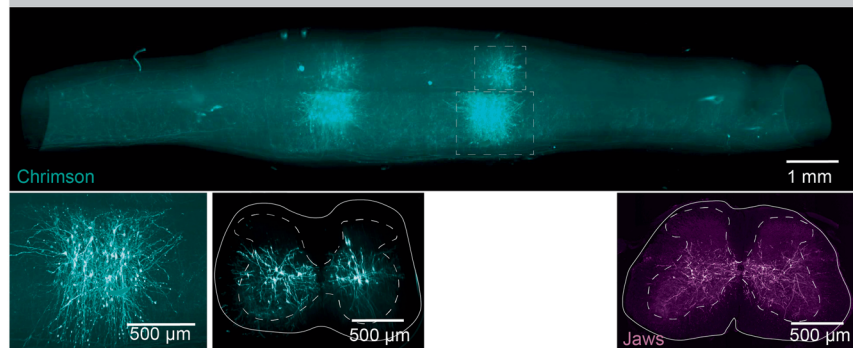
Step 1: Timeline of experiment



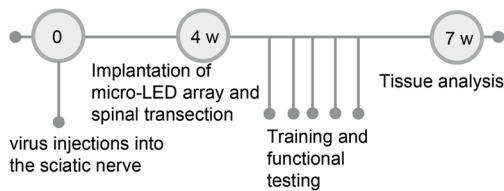
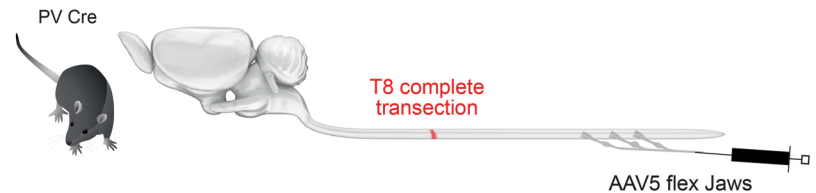
Step 2: Intersectional genetics to target the V2a Interneurons



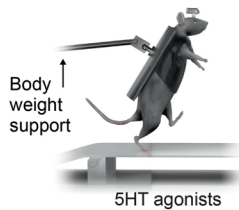
Step 3: Post-mortem verification of Chrimson and Jaws expression

b Silencing PV^{ON} sensory afferents

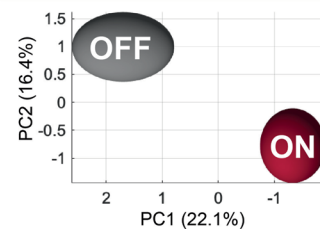
Step 1: Timeline of experiment

Step 2: Intersectional genetics to target the PV^{ON} afferent fibers

Step 3: Functional testing



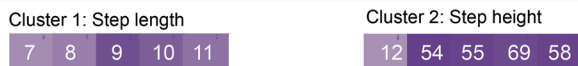
Step 4: Kinematic analysis



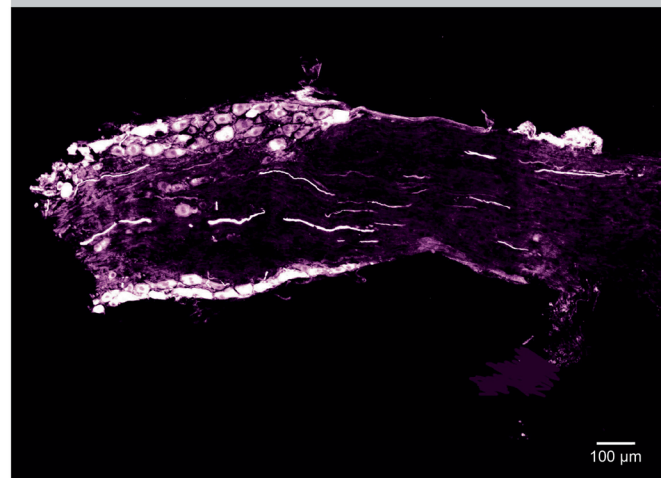
Step 5: Factor loadings of gait parameters onto PC1



Step 6: Functional clusters to identify the most affected variables



Step 7: Post-mortem verification of Jaws expression



Extended Data Fig 10 | Intersectional genetics to target specific neurons in the spinal cord and dorsal root ganglia. **a**, Manipulation of V2a interneurons during swimming. **Step 1:** Timeline detailing key experiments. **Step 2:** Schematic illustration of the experimental procedures to express ChrimsonR in V2a interneurons with targeted injection of virus in the lumbar spinal cord of Vsx2 Cre mice. **Step 3:** Post-mortem verification of Jaws or Chrimson expression. 3D images, including coronal sections showing the robust expression of Jaws or ChrimsonR in the lumbar spinal cord. **b**, Silencing PV^{ON} neurons in afferent fibers. **Step 1:** Timeline detailing key experiments. **Step 2:** Schematic illustration of the experimental procedures to express Jaws in PV^{ON} located in the dorsal root ganglia using targeted injection of virus in the sciatic nerve. **Step 3:** Experimental setup to record leg kinematics during stepping on a treadmill in mice with complete SCI. A serotonergic pharmacotherapy is administered prior to the experiment to reactivate the lumbar spinal cord below the injury. **Step 4:** A series of 78 gait parameters (see Supplementary Table 1) calculated from the kinematic recordings are submitted to a PC analysis. Each dot represents the mean and SEM values of many gait cycles ($n > 10$ pre mouse) are shown in the new denoised space defined by PC1 and PC2. **Step 5:** Factor loadings of individual parameters on PC1 (correlation between PC1 and each variable). **Step 6:** Functional clusters of highly correlated parameters were extracted from PC1 loadings representing gait parameters that describe differences between groups the most. Parameters relating to step length and height explained a large variance of the gait cycles, therefore indicating it best describes differences between groups. **Step 7:** Post-mortem verification of Jaws expression. Photographs show the robust expression of Jaws in PV^{ON} located in the dorsal root ganglia and sciatic nerve.

Reporting Summary

Nature Research wishes to improve the reproducibility of the work that we publish. This form provides structure for consistency and transparency in reporting. For further information on Nature Research policies, see our [Editorial Policies](#) and the [Editorial Policy Checklist](#).

Statistics

For all statistical analyses, confirm that the following items are present in the figure legend, table legend, main text, or Methods section.

n/a Confirmed

- The exact sample size (n) for each experimental group/condition, given as a discrete number and unit of measurement
- A statement on whether measurements were taken from distinct samples or whether the same sample was measured repeatedly
- The statistical test(s) used AND whether they are one- or two-sided
Only common tests should be described solely by name; describe more complex techniques in the Methods section.
- A description of all covariates tested
- A description of any assumptions or corrections, such as tests of normality and adjustment for multiple comparisons
- A full description of the statistical parameters including central tendency (e.g. means) or other basic estimates (e.g. regression coefficient) AND variation (e.g. standard deviation) or associated estimates of uncertainty (e.g. confidence intervals)
- For null hypothesis testing, the test statistic (e.g. F , t , r) with confidence intervals, effect sizes, degrees of freedom and P value noted
Give P values as exact values whenever suitable.
- For Bayesian analysis, information on the choice of priors and Markov chain Monte Carlo settings
- For hierarchical and complex designs, identification of the appropriate level for tests and full reporting of outcomes
- Estimates of effect sizes (e.g. Cohen's d , Pearson's r), indicating how they were calculated

Our web collection on [statistics for biologists](#) contains articles on many of the points above.

Software and code

Policy information about [availability of computer code](#)

Data collection Data were collected using Labchart v8 (ADInstruments), Labview (2018 version 18.0), Zen2 Black (Zeiss), Imaris (9.1.2, 64Bit, Bitplane).

Data analysis All softwares and software versions used to analyze data are described in the Method section at the relevant paragraph. Following is a list of softwares used: Imaris (Bitplane, v.9.0.0), ImageJ NIH, Labchart, MATLAB, itk SNAP, AnalyzeDirect, Inc., USA, Sim4Life by ZMT, COMSOL Multiphysics® v. 5.3., Matrox Solios eCL-B, Arivis AG, Munich, Germany, Neurolucida MBF Bioscience. Illustrations were generated using Autodesk 2020.2, Maya 2020.2, Adobe Illustrator CC 2015. R (version 3.6.0), PRISM version 8.3 (GraphPad).

For manuscripts utilizing custom algorithms or software that are central to the research but not yet described in published literature, software must be made available to editors and reviewers. We strongly encourage code deposition in a community repository (e.g. GitHub). See the Nature Research [guidelines for submitting code & software](#) for further information.

Data

Policy information about [availability of data](#)

All manuscripts must include a [data availability statement](#). This statement should provide the following information, where applicable:

- Accession codes, unique identifiers, or web links for publicly available datasets
- A list of figures that have associated raw data
- A description of any restrictions on data availability

Data that support the findings will be made available upon reasonable request to the corresponding author.

Field-specific reporting

Please select the one below that is the best fit for your research. If you are not sure, read the appropriate sections before making your selection.

Life sciences Behavioural & social sciences Ecological, evolutionary & environmental sciences

For a reference copy of the document with all sections, see [nature.com/documents/nr-reporting-summary-flat.pdf](https://www.nature.com/documents/nr-reporting-summary-flat.pdf)

Life sciences study design

All studies must disclose on these points even when the disclosure is negative.

Sample size	Sample sizes are estimated based on previous studies using similar animal models and implants. Knowing the typical variance of behavioural effects and histological quantitative analyses, we estimated that n=5 to 10 animals per group allows at least 80% statistical power when using the appropriate statistical test for assessing the effects of array implantation. When assessing the behavioural effects due to photostimulation, n ≥ 3 was used per condition. The comparisons were performed intra-animal.
Data exclusions	Expression of viral vectors were confirmed post-mortem. If there was a lack of expression, the animal was excluded from behavioural analysis.
Replication	All tested conditions were repeated across multiple trials and the results averaged to obtain a single-subject mean performance where applicable.
Randomization	For in vivo measurements relating to temperature increase, we randomized the order of conditions. For all behavioural testing, we randomized trials with and without photostimulation.
Blinding	In some cases blinding is not possible during data collection as the photostimulation is visible. However, all statistical analysis was completed with the investigator blind to the experimental codings.

Reporting for specific materials, systems and methods

We require information from authors about some types of materials, experimental systems and methods used in many studies. Here, indicate whether each material, system or method listed is relevant to your study. If you are not sure if a list item applies to your research, read the appropriate section before selecting a response.

Materials & experimental systems

Methods

n/a	Involved in the study
<input type="checkbox"/>	<input checked="" type="checkbox"/> Antibodies
<input checked="" type="checkbox"/>	<input type="checkbox"/> Eukaryotic cell lines
<input checked="" type="checkbox"/>	<input type="checkbox"/> Palaeontology and archaeology
<input type="checkbox"/>	<input checked="" type="checkbox"/> Animals and other organisms
<input checked="" type="checkbox"/>	<input type="checkbox"/> Human research participants
<input checked="" type="checkbox"/>	<input type="checkbox"/> Clinical data
<input checked="" type="checkbox"/>	<input type="checkbox"/> Dual use research of concern

n/a	Involved in the study
<input checked="" type="checkbox"/>	<input type="checkbox"/> ChIP-seq
<input checked="" type="checkbox"/>	<input type="checkbox"/> Flow cytometry
<input type="checkbox"/>	<input checked="" type="checkbox"/> MRI-based neuroimaging

Antibodies

Antibodies used	The following primary and secondary antibodies were used: rabbit anti-GFAP (1:1000, Dako Z0334), anti-Iba1 (1:1000, FUJIFILM Wako 019-19741), Alexa Fluor Conjugated, Invitrogen.
Validation	The concentration of each antibody was tested before use and confirmed based on the morphology of positive signal.

Animals and other organisms

Policy information about [studies involving animals](#); [ARRIVE guidelines](#) recommended for reporting animal research

Laboratory animals	Experiments were conducted on adult male or female C57BL/6 mice (18-35g body weight, 8-25 weeks of age). Thy1::Chr2 (Jackson Laboratory 12350), vGluT2 Cre (Jackson Laboratory 016963), Parvalbumin Cre (Jackson Laboratory 017320) and Vsx2 Cre (MMMRRC 36672, also called Chx10 Cre) transgenic mouse strains were used and maintained on a mixed genetic background (C57BL/6).
Wild animals	This study did not involve wild animals.
Field-collected samples	The study did not involve samples collected from the field.
Ethics oversight	Procedures and surgeries were approved by the Veterinary Office of the Canton of Geneva (Switzerland; GE/51/20).

Magnetic resonance imaging

Experimental design

Design type	The MRI was performed post-mortem as a high-resolution structural scan.
Design specifications	n/a
Behavioral performance measures	n/a

Acquisition

Imaging type(s)	structural
Field strength	9.4T
Sequence & imaging parameters	Anatomical images were acquired using a fast spin-echo sequence (in-plane resolution: 47 x 47 μm^2 , FOV: 12x12 mm ² , matrix size: 192x192 zero-filled to 256x256, slice thickness: 0.5 mm, 20 slices, TE/TR = 13/5000 ms, echo train length: 4, TE _{eff} = 13 ms, 24 averages, scan time = 1h36min).
Area of acquisition	lumbar spinal cord of the mouse
Diffusion MRI	<input type="checkbox"/> Used <input checked="" type="checkbox"/> Not used

Preprocessing

Preprocessing software	n/a
Normalization	n/a
Normalization template	n/a
Noise and artifact removal	n/a
Volume censoring	n/a

Statistical modeling & inference

Model type and settings	n/a
Effect(s) tested	n/a
Specify type of analysis:	<input type="checkbox"/> Whole brain <input type="checkbox"/> ROI-based <input type="checkbox"/> Both
Statistic type for inference (See Eklund et al. 2016)	n/a
Correction	n/a

Models & analysis

n/a	Involved in the study
<input checked="" type="checkbox"/>	<input type="checkbox"/> Functional and/or effective connectivity
<input checked="" type="checkbox"/>	<input type="checkbox"/> Graph analysis
<input checked="" type="checkbox"/>	<input type="checkbox"/> Multivariate modeling or predictive analysis